Thesis for the Degree of Master of Engineering

Estimation of Initial Seabed Settlement of Artificial Reefs according to Installation Velocities

by

Min Ji Kim

Department of Ocean Engineering

The Graduate School

Pukyong National University

February 23, 2018

Estimation of Initial Seabed Settlement of Artificial Reefs according to Installation Velocities

인공어초 설치 속도에 따른 초기 침하량 산정

Advisor: Prof. Won-Bae Na

by

Min Ji Kim

A thesis submitted in partial fulfillment of the requirements
for the degree of

Master of Engineering

in Department of Ocean Engineering, The Graduate School,
Pukyong National University

February 2018

Estimation of Initial Seabed Settlement of Artificial Reefs according to Installation Velocities

A dissertation

by

Min Ji Kim

Approved by:

_____

(Chairman) Kim, Jeong-Tae

_____ _____

(Member) Yoon, Han-Sam (Member) Na, Won-Bae

February 23, 2018

TABLE OF CONTENTS

LIST OF FIGURES

LIST OF TABLES

Estimation of Initial Seabed Settlement of Artificial Reefs according to Installation Velocities

Min Ji Kim

Department of Ocean Engineering,
The Graduate School,
Pukyong National University

ABSTRACT

인공어초를 설치할 때 일반적으로 선박에서 자유낙하를 시키거나 케이블을 이용한다. 이 때, 인공어초와 해저지반의 충돌로 인해 초기 침하가 발생할 수 있으며 이것은 인공어초의 공용적 감소로 이어진다. 본 연구는 동적 유한요소 해석프로그램인 ANSYS-AUTODYN을 사용하여 인공어초의 설치 중 발생할 수 있는 해저지반의 초기침하량을 해석하였다. 해석 대상은 국내 연안에 가장 많이 설치된 사각어초와 반구형어초이다. 해석변수로는 설치 속도(0.2m/s, 0.4m/s, 0.6m/s)와 지반모델(진흙이 섞인 포화된 모래지반, 자갈이 섞인 포화된 모래지반)을 고려하였다. 사각어초는 추가적으로 설치 각도(θ = 5°, 10°, 15°)를 고려하여 해저지반의 초기침하를 정량화하였다. 모든 해저지반에서, 어초의 종류와 관계없이 설치 속도가 빠를수록 초기침하가 크게 나타났지만 그 차이는 크지 않았다. 자갈이 섞인 포화된 모래지반에 비해 진흙이 섞인 포화된 모래지반에서 초기침하가 상당히 크게 나타났다. 사각어초와 반구형어초 모두 약 39cm의 침하가 발생하였다. 유효공용적의 손실률을 산정해보면 사각어초는 약 20%, 반구형어초는 약 41%가 발생하였다.

CHAPTER 1
INTRODUCTION

1.1 Background

Artificial reefs (ARs), man-made structures, are installed for the following purposes: reducing beach erosion, protecting marine habitats, and providing recreational fishing and diving sites (Han, 2016; Düzbastılar and Şentürk, 2009).

Generally, ARs are installed on the seabed using a free fall method or a guided way through a cable or wire (Yoon *et al.*, 2016). Nowadays, the cable method is recommended for most installation activities because this method can locate the target seabed in exacter manner than the free fall method. However, even with careful installation with the cables, AR deployment may cause the initial settlement of the seabed. This may cause initial settlement of the AR. The settlement of AR can cause a problem in terms of efficiency and stability (Kim *et al.*, 2009).

Regarding the settlement, most studies concentrate on scour, partial and total settlement of ARs already installed. There are few studies on the initial settlement by collision between ARs and the seabed during installation. Therefore, it is necessary to investigate the immediate settlement.

1.2 Objective and Scope

This study investigates the initial settlement of ARs according to installation velocity and seabed soil properties and compositions.

First, a cube-type reef and a half-ball type reef were selected. This was selected based on the amount of ARs installed in the Korean coastal waters. Second, three installation velocities were selected. The installation velocity at which the ARs are installed is not known exactly. The installation velocity used for calculating the impact force at collision between the seabed and the AR is generally 1.0m/s (Kim et al., 2008), so the installation velocity is arbitrarily set to a value less than 1.0m/s. In this study, 0.2m/s, 0.4m/s, and 0.6m/s were set as installation velocities. Third, two seabed soil conditions were selected. It is the seabed composed of saturated sand (70%) and gravel (30%) and saturated sand (85%) and clay (15%).

A total of 12 cases were investigated for two ARs, two seabed soil conditions, and three installation velocities. In addition, three installation angles (5˚, 10˚, 15˚) were also considered in case of a cube-type reef. The scope and method are summarized in Fig. 1.1.

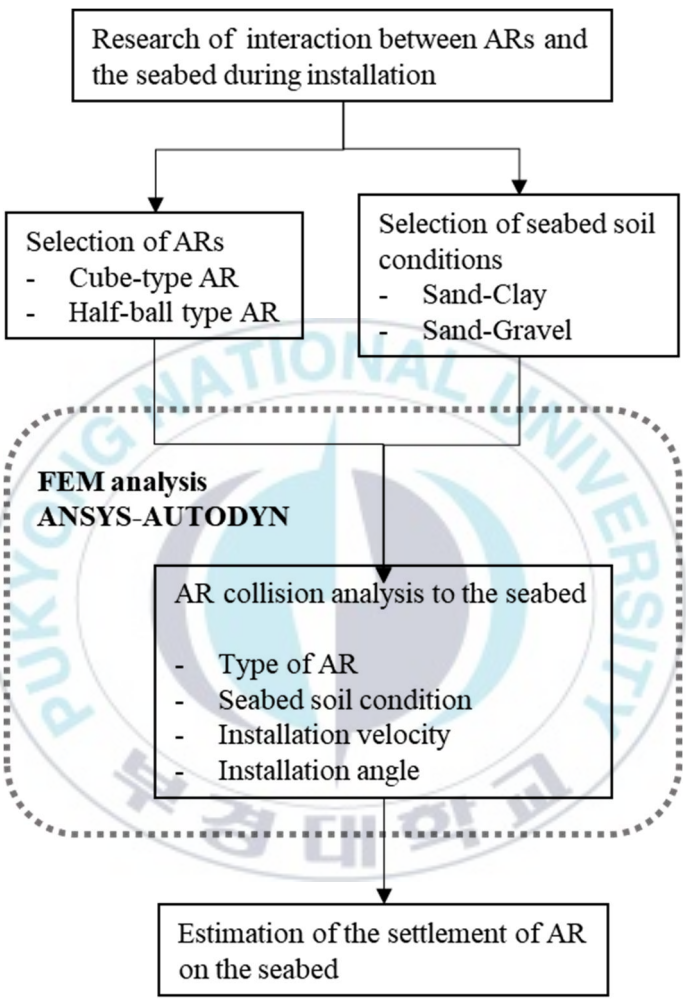

Fig. 1.1. Flow chart of this study.

CHAPTER 2
MATERAIL AND METHODS

2.1 Target Artificial Reefs

In Korea, 72 general ARs have been approved by the central Artificial Reef Committee since 1971 (Woo *et al.*, 2014). Among them, the ARs used in this study were selected considering the installed amount. Cube-type ARs about 936,776 and half-ball type ARs about 132,163 have been installed in Korean coastal waters from 1971 to 2016 (Korea Fisheries Resources Agency, 2017b). These ARs are the two most installed. Figure 2.1 and Figure 2.2 show the cube-type reef and the half-ball type reef which are considered this study.

The cube-type AR is made of concrete and reinforcing bars. It has dimensions of 2m (B) × 2m (L) × 2m (H), for an apparent facility volume of 8m^3, and a weight of 33.34kN (3.4tons). The thickness of the horizontal and vertical members is all 0.25m. It is classified as an AR for fish and has features such as simple shape, easy to make and cheap (FIRA, 2017a; Jung *et al.*, 2016). A modified model is used, as shown in Fig. 2.3, in this study because the inner edges in Fig. 2.1 does not have effect on collision analysis.

The half-ball type AR is made of concrete and reinforcing bars. It has dimensions of 2m (B) × 2m (L) × 1.3m (H), for an apparent facility volume of 3m^3, and a weight of 21.57kN (2.2tons). The thickness is 0.15m. It is classified as an AR for shellfish and seaweed (FIRA, 2017a) and is regarded the most popular type in marine forest AR.

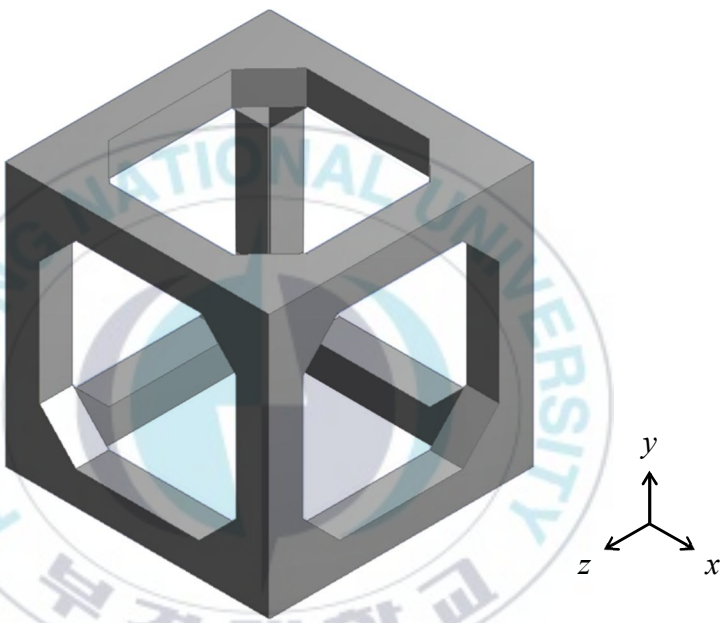

Fig. 2.1. A cube-type reef.

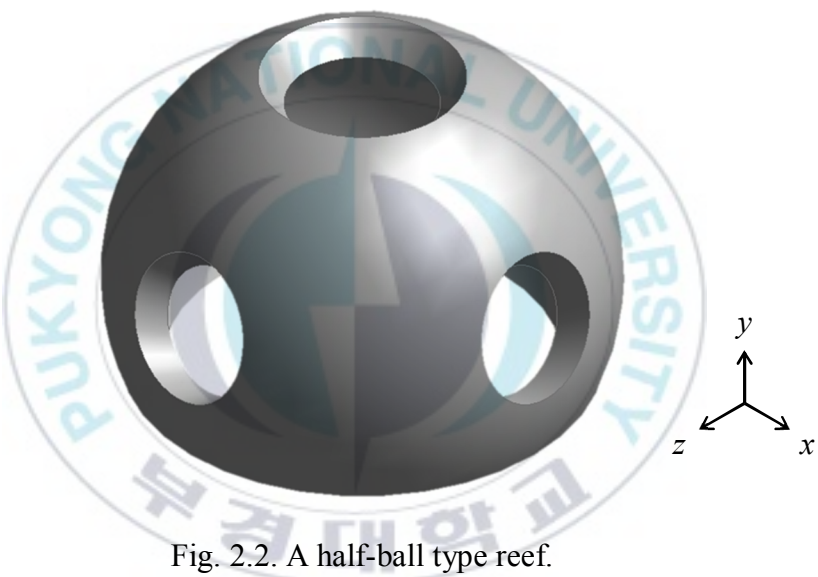

Fig. 2.2. A half-ball type reef.

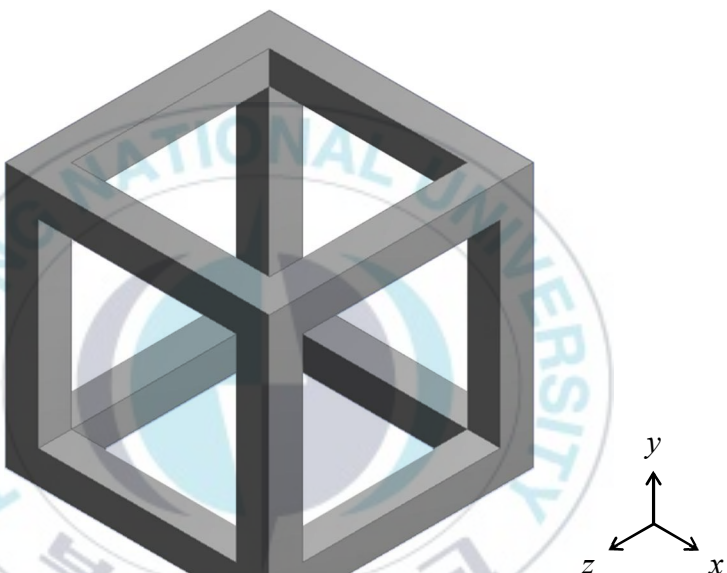

Fig. 2.3. Modified cube-type reef.

2.2 Explicit Dynamics

2.2.1 ANSYS-AUTODYN

The most accurate method for estimating the deformation and state change of a solid caused by a collision is an experiment-based method. However, the response of the structure caused by the collision occurs within a very short time, and consequently it is not easy to carry out the experiment realistically. Therefore, in this study, collision analysis between the AR and the seabed is performed using an explicit dynamic analysis software package ANSYS-AUTODYN.

2.2.2 Governing equations

In finite element analysis, the mass of one element is constant, and the initial mass is retained in the deformation of the volume, such as distortion. Thus, in the software package, the density of the material can be expressed as Eq. 2.1.

$$\rho = \frac{\rho_0 V_0}{V} = \frac{m}{V} \tag{2.1}$$

Here, ρ_0 is an initial density and V_0 is an initial volume.

Equations of momentum conservation are expressed with regard to acceleration ($\rho\ddot{x}$, $\rho\ddot{y}$, $\rho\ddot{z}$) and stress tensor (σ_{ij}) as Eq. 2.2.

$$\rho\ddot{x} = \frac{\partial\sigma_{xx}}{\partial x} + \frac{\partial\sigma_{xy}}{\partial y} + \frac{\partial\sigma_{xz}}{\partial z} \tag{2.2a}$$

$$\rho\ddot{y} = \frac{\partial\sigma_{yx}}{\partial x} + \frac{\partial\sigma_{yy}}{\partial y} + \frac{\partial\sigma_{yz}}{\partial z} \tag{2.2b}$$

$$\rho\ddot{z} = \frac{\partial\sigma_{zx}}{\partial x} + \frac{\partial\sigma_{zy}}{\partial y} + \frac{\partial\sigma_{zz}}{\partial z} \tag{2.2c}$$

Energy conservation equations used in AUTODYN can be expressed in a strain rate and stress tensor as Eq. 2.3. The strain rate, $\dot{\varepsilon}_{ij}$, is determined from the relation between strain rates and velocities ($\dot{x}, \dot{y}, \dot{z}$) and it can be expressed as Eq. 2.4.

$$\dot{e} = \frac{1}{\rho}\left(\sigma_{xx}\dot{\varepsilon}_{xx} + \sigma_{yy}\dot{\varepsilon}_{yy} + \sigma_{zz}\dot{\varepsilon}_{zz} + 2\sigma_{xy}\dot{\varepsilon}_{xy} + 2\sigma_{yz}\dot{\varepsilon}_{yz} + 2\sigma_{zx}\dot{\varepsilon}_{zx}\right) \tag{2.3}$$

$$\dot{\varepsilon}_{xx} = \frac{\partial \dot{x}}{\partial x} \tag{2.4a}$$

$$\dot{\varepsilon}_{yy} = \frac{\partial \dot{y}}{\partial y} \tag{2.4b}$$

$$\dot{\varepsilon}_{zz} = \frac{\partial \dot{z}}{\partial z} \tag{2.4c}$$

$$\dot{\varepsilon}_{xy} = \frac{1}{2}\left(\frac{\partial \dot{x}}{\partial y} + \frac{\partial \dot{y}}{\partial x}\right) \tag{2.4d}$$

$$\dot{\varepsilon}_{yz} = \frac{1}{2}\left(\frac{\partial \dot{y}}{\partial z} + \frac{\partial \dot{z}}{\partial y}\right) \tag{2.4e}$$

$$\dot{\varepsilon}_{zx} = \frac{1}{2}\left(\frac{\partial \dot{z}}{\partial x} + \frac{\partial \dot{x}}{\partial z}\right) \tag{2.4f}$$

2.3 Modeling

A cube-type reef is modeled as shown in Fig. 2.4 with hexahedron elements and mesh size is determined by 0.5m. A half-ball type reef modeled as shown in Fig. 2.5 with hexahedron and tetrahedron elements. And mesh size is determined to be smaller than 0.5m. The seabed is modeled as shown in Fig. 2.6. The length, width, and height of the seabed are 8m, 8m, and 2m, respectively and hexahedron elements are used. Element size of inner part, collision with the AR, is determined by 0.05m and element size of the others part is determined by 0.2m.

The locations of gauges for a cube-type reef when installation angle is 0˚, 5˚, 10˚, and 15˚ are as shown in Fig. 2.7 and 2.8. The locations of gauges for a half-ball type reef are as shown in Fig. 2.9.

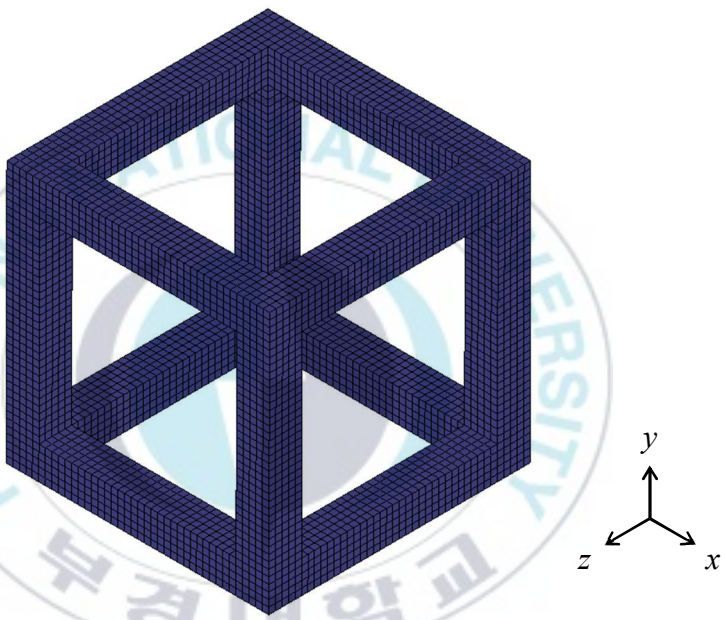

Fig. 2.4. Modeled cube-type reef.

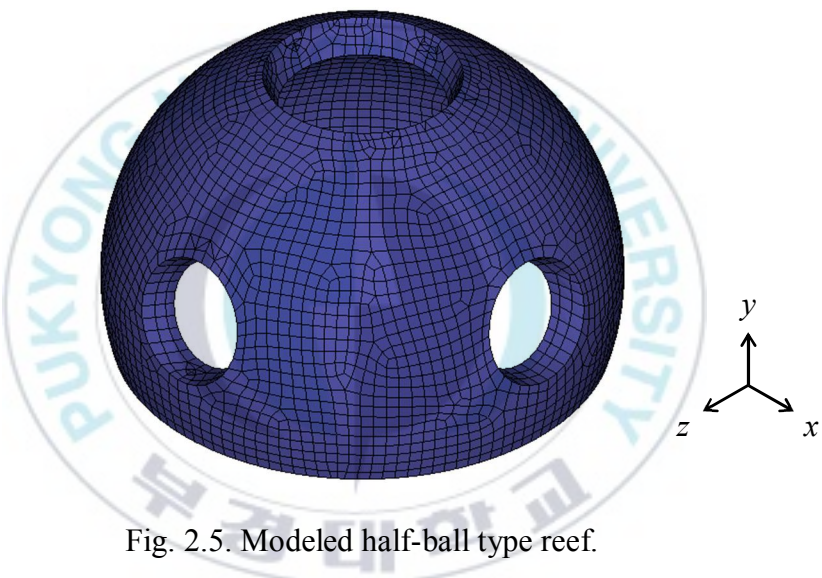

Fig. 2.5. Modeled half-ball type reef.

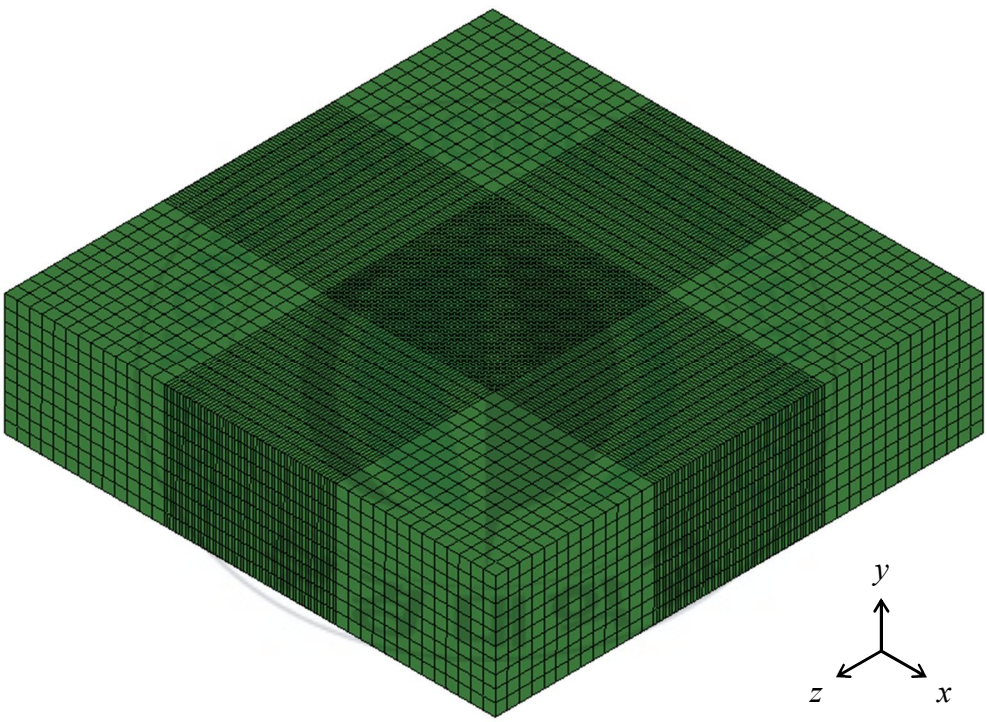

Fig. 2.6. Modeled seabed.

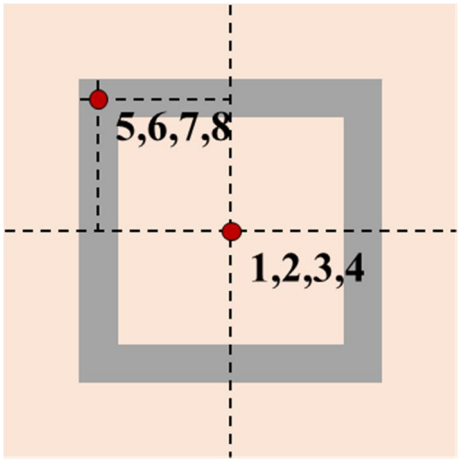

(a) top view

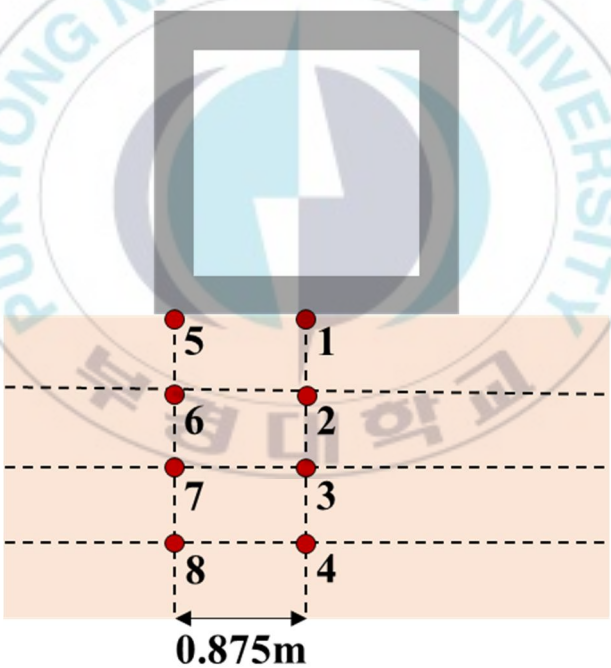

(b) front view

Fig. 2.7. The locations of gauges for a cube-type reef when installation angle is 0˚.

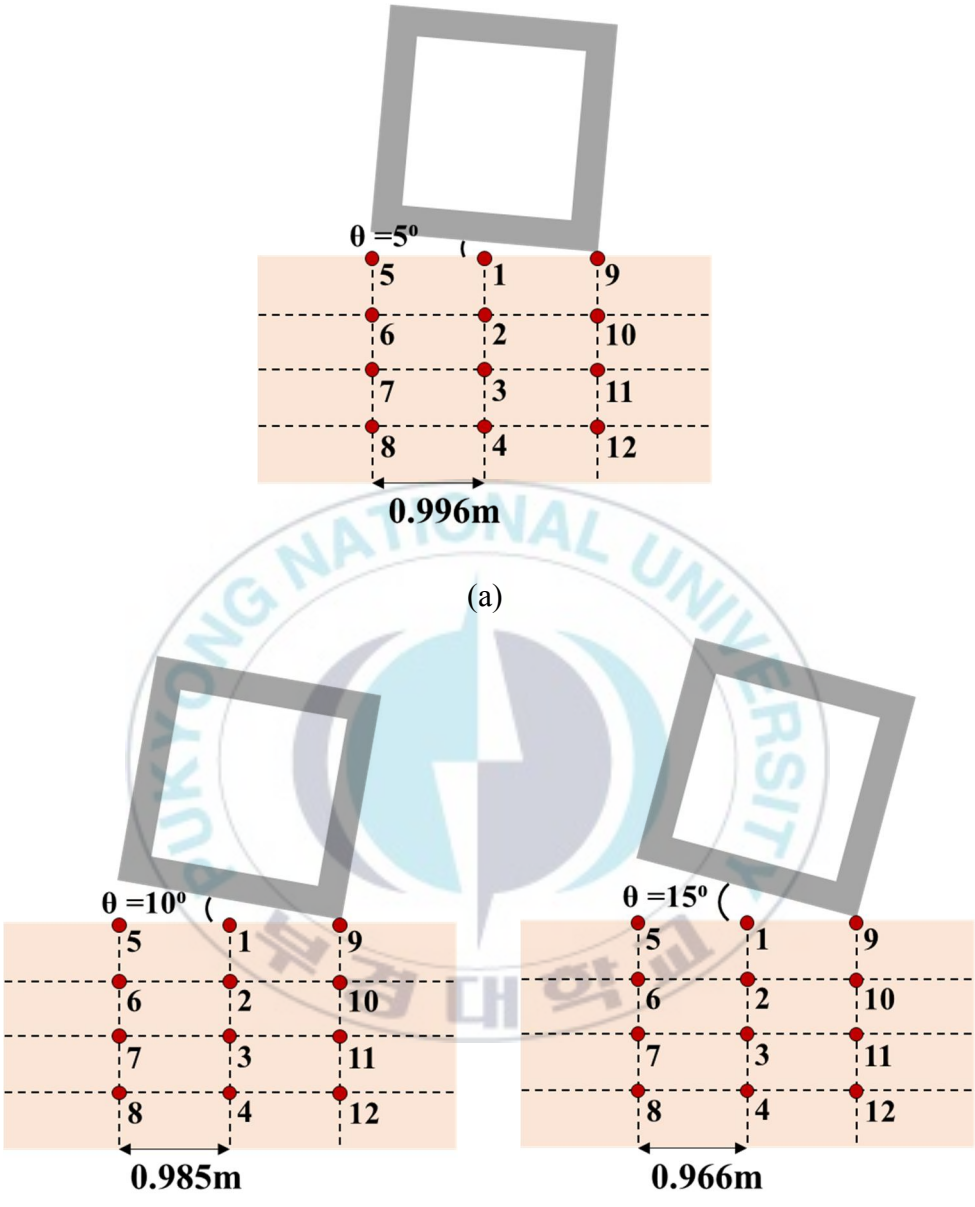

(b) (c)

Fig. 2.8. The locations of gauges for a cube-type reef: (a) θ = 5˚, (b) θ = 10˚, and (c) θ = 15˚.

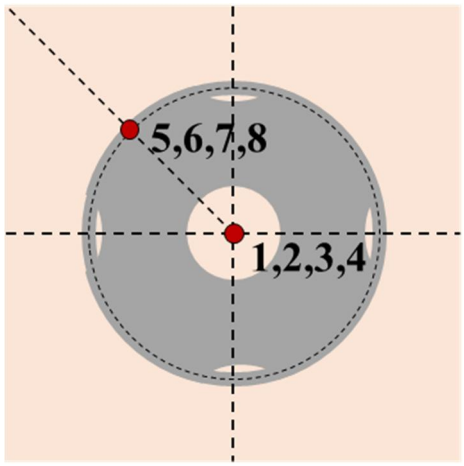

(a) top view

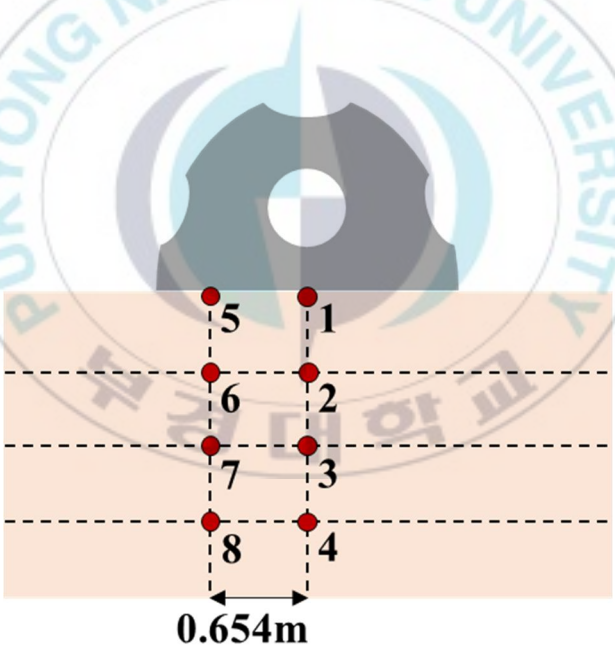

(b) front view

Fig. 2.9. The locations of gauges for a half-ball type reef.

2.4 Material Model

2.4.1 RHT concrete model

Although the cube-type reef and the half-ball type reef are made by concrete and reinforcing bars, in this study, it was assumed that the ARs are made of concrete only because we focused on the settlement of the seabed by the AR. Thus, the RHT concrete model proposed by Riedel, Hiermaier, and Thoma (1999) was used because it is a concrete model mainly used for high-speed collisions such as shell impact. It constructs the material model by substituting the material constants of the concrete into equations (Woo *et al*, 2009). Material properties of the RHT concrete model used in this study are shown in Table 2.1.

In the ANSYS AUTODYN, the equation of state, strength equation, failure equation, and erosion criteria are required to express a material characteristic. The RHT concrete model is composed of a *P-α* equation of state, RHT strength equation, RHT failure equation, and erosion criteria based on geometric distortion (ANSYS Inc., 2009).

P-α equation of state can be expressed as Eq. 2.5. It is generally used to describe the dynamic condition of concrete with changes in pressure.

$$P = f(\rho\alpha, e) = \ A_1\mu + A_2\mu^2 + A_3\mu^3 + (B_0 + B_1\mu)\rho_0 e \tag{2.5}$$

Here, A_1, A_2, A_3, B_0, and B_1 are material coefficients, ρ_0 is the initial density of material, e is internal energy, and $\mu = \frac{\rho}{\rho_0} - 1$ is a changes in relative volume of material. The porosity α can represents as Eq. 2.6.

$$\alpha = 1 + (\alpha_{init} - 1)\left[\frac{P_{lock} - P}{P_{lock} - P_{crush}}\right]^{n} \tag{2.6}$$

Here, α_{init} is an initial porosity of the concrete, P_{lock} is a pressure when porosity of the concrete is α_{init}, and P_{crush} is a pressure when porosity of the concrete is zero.

In concrete, tensile strength is weak and failure occurs in small tensile deformation. RHT strength model is expressed in terms of the initial elastic yield surface, the failure surface, and the residual friction surface as Eq. 2.7 (Borrvall and Riedel, 2011).

$$Y_{fail}(P, \theta, \dot{\varepsilon}) = Y_{TXC}(P) F_{Rate}(\dot{\varepsilon}) R_3(\theta) \tag{2.7a}$$

$$Y_{TXC}(P) = f_c A\left[P^* - P^*{}_{spall} F_{Rate}\right]^N \tag{2.7b}$$

$$F_{Rate}(\dot{\varepsilon}) = \begin{cases} \left(\frac{\dot{\varepsilon}}{\dot{\varepsilon}_0}\right)^{\alpha} & for\ P > \frac{1}{3} f_c, with\ \dot{\varepsilon}_0 = 30 \times 10^{-6} s^{-1} \\ \left(\frac{\dot{\varepsilon}}{\dot{\varepsilon}_0}\right)^{\delta} & for\ P < \frac{1}{3} f_c, with\ \dot{\varepsilon}_0 = 3 \times 10^{-6} s^{-1} \end{cases} \tag{2.7c}$$

$$R_3(\theta) = \frac{2\left(1 - {Q_2}^2\right)cos^2\theta + (2Q_2 - 1)\left[4\left(1 - {Q_2}^2\right)cos^2\theta + 5{Q_2}^2 - Q_2\right]^{\frac{1}{2}}}{4\left(1 - {Q_2}^2\right)cos^2\theta + (1 + Q_2)^2}, \tag{2.7d}$$

with $Q_2 = Q_{2,0} + BQP^*$

Here, f_c is compressive strength of concrete, *A* and *N* are coefficients for defining the failure surface, P^* is the nominalized pressure by compressive strength, $P^*{}_{spall}$ is the nominalized spall strength by compressive strength, θ is the load angle given by the deviatoric stress tensor, Q_2 is maximum reduction in strength, $Q_{2,0}$ is maximum reduction

in strength when pressure is zero, and BQ is a coefficient indicating the change of the fracture surface due to the increase in pressure.

The RHT failure model is expressed by Eq. 2.8. Damage level (D) is expressed in terms of plastic strain (ε_p) and failure stain ($\varepsilon_p^{failure}$) - pressure dependent with a material coefficient (D_1 and D_2) as shown by Eq. 2.9. The residuals strength ($Y^*_{residure}$) is expressed by the pressure and material constants denoted by B and M, as Eq. 2.10. The fracture surface of the material can be expressed by the residual strength and fracture strength owing to damage as Eq. 2.11.

$$D = \sum \frac{\Delta \varepsilon_p}{{\varepsilon_p}^{failure}} \tag{2.8}$$

$${\varepsilon_p}^{failure} = D_1 \left(P^* - {P^*}_{spall}\right)^{D_2} \tag{2.9}$$

$${Y^*}_{residure} = B(P^*)^M \tag{2.10}$$

$${Y^*}_{fracture} = (1-D){Y^*}_{failure} + D{Y^*}_{residure} \tag{2.11}$$

Table. 2.1. Material properties of RHT concrete model

Parameter	Value
Porous density (kg/mm^3)	2.0×10^6
Porous sound speed (m/s)	2920
Initial compaction pressure (MPa)	23.3
Solid compaction pressure (GPa)	6.0
Compaction exponent	3
Bulk modulus *A1*	3.527×10^7
Parameter *A2*	3.958×10^7
Parameter *A3*	9.04×10^6
Parameter *B0*	1.22
Parameter *B1*	1.22
Shear modulus (GPa)	16.7
Compressive strength (MPa)	35.0
Tensile strength (ft/fc)	0.1
Shear strength (ft/fc)	0.18
Intact failure surface constant *A*	1.6
Intact failure surface exponent *N*	0.61
Brittle to ductile transition	0.0105
Fractured strength constant *B*	1.6
Fractured strength exponent *M*	0.61
Damage constant D_1	0.04
Damage constant D_2	1
Principal tensile failure stress (MPa)	5
Fracture energy (J/m^2)	120
Erosion strain	1.5

2.4.2 CU-ARL model

The seabed soil is composed of a variety of materials such as sand, clay, silt, and gravel *etc*. The seabed is very complicated material because particle sizes, particle size distribution, and moisture content can profoundly affect the soil properties.

Compaction model proposed by Laine and Sandvik (2001) was developed for dry sand, so cannot account for the effects of moisture, clay and/or gravel in soil (Grujicic and Bell, 2011). To resolve the problem of the original compaction model, Clemson University (CU) and Army Research Laboratory (ARL) developed and parameterized the new sand model which was named the CU-ARL sand model. The CU-ARL sand model contains all the basic ingredient required for soil model and may include a model containing clay or a model containing graver. Therefore, in this study, the CU-ARL sand model is considered as the material condition of the seabed soil.

The CU-ARL sand model is composed of compaction model, MO Granular strength model, *Pmin* failure model, and erosion criteria based on geometric distortion (Grujicic and Bell, 2011). Material properties of the seabed model used in this study are shown in Table 2.2 and 2.3 (Grujicic and Bell, 2011), respectively.

The CU-ARL sand equation of state is based on the following assumptions (Grujicic *et al*., 2008): (1) the dynamic mechanical response of the sand at any degree of saturation can be obtained as a linear combination of the corresponding dynamic material behaviors for the dry and saturated sand; (2) the initial density of the saturated sand can be obtained by the density of sand (ρ_s), density of water (ρ_w), and initial porosity (α_o); (3) when

saturated sand is under the relatively low deformation rate, fully compacted sand and the pressure are identical to dry sand; (4) when the saturated sand is under high compression rate, the compressibility of saturated sand is controlled by the compressibility of its solid condition; and (5) when the saturated sand is under the intermediate deformation rate, the density of saturated sand can obtained using interpolation procedure as $\rho = \rho_{high} + (\rho_{low} - \rho_{high})\left(\frac{\log\dot{\varepsilon} - \log\dot{\varepsilon}_{high}}{\log\dot{\varepsilon}_{low} - \log\dot{\varepsilon}_{high}}\right)$, where the density ρ, ρ_{high}, ρ_{low} correspond respectively to the deformation rates $\dot{\varepsilon}$, $\dot{\varepsilon}_{high}$, and $\dot{\varepsilon}_{low}$, and are all associated with the same level of pressure.

The equation of state is composed by relation of Pressure *vs.* density, and speed of sound *vs.* density. The equation of state of the CU-ARL sand model is expressed in Eq. 2.12 (Grujicic *et al.*, 2008). Here, $\rho_0 = (1-\alpha_0)\rho_{ref} + \alpha_0\beta_0\rho_w$ is an initial mass density, ρ_{ref} is reference density of sand, *s* is the parameter, α_0 is an initial porosity level of sand, β_0 is initial saturation ratio, ρ_w is water density, C_0 is sound speed, and *s* is an increasing rate of the average particles velocity. Equation 2.13 is an expression of the density of the sand at full compaction. Here, it should be noted that C_0 and *s* is obtained by results in Bragov *et al*. (2008) and Chapman *et al*. (2006). According to results of Grujicic *et al*. (2007), saturated sand has the uniformed speed of sound.

$$P = \begin{cases} \dfrac{\rho_0 {C_0}^2 \eta}{(1-s\eta)^2} & \rho \le \rho_{comp} \\ \rho_{comp} + {C_0}^2(1-\rho_{comp}) & \rho > \rho_{comp} \end{cases} \tag{2.12}$$

$$\rho_{comp} = \left(\frac{1-\alpha_0}{1-\alpha_0\beta_0}\right)\rho_{ref} + \left(\frac{\alpha_0\beta_0}{1-\alpha_0+\alpha_0\beta_0}\right)\rho_w \tag{2.13}$$

The CU-ARL sand strength model is based on the following assumption (Grujicic *et al*., 2008): (1) strength model is used when sand is based on as isotropic, perfectly plastic, rate independent, yield surface approximation, and yield strength depends on pressure, not on density; (2) the deviatoric stress is proportional to the deviatoric strain with the proportionality constant being equal to shear modulus, *G*. The shear modulus is depending on density of material which has natural porosity; and (3) the water inside sand creates water-based shear layer physically separating sand particles and reduces the effective friction coefficient.

In original compaction strength model for dry sand, the yield stress is assumed to be controlled by inter-particle friction. In research of Grujicic *et al*. (2008), the strength model for saturated sand is expressed by Eq. 2.14. Here, P_{MC} (1.864×10^5kPa) is the Mohr-Coulomb pressure and ϕ_{sat} is proportionality coefficient about yield stress and pressure as shown in Eq. 2.15.

$$\sigma_{y,sat} = \phi_{sat} P_{sat} \approx \begin{cases} \phi_{sat} P_{sat} & P_{dry}, 0 < P_{dry} \le P_{MC} \\ \phi_{sat} P_{MC} & P_{dry} > P_{MC} \end{cases} \quad (2.14)$$

$$\phi_{sat} = \begin{cases} 0.1 + 1.2732 \dfrac{P_{dry}}{P_{MC}} & P_{dry}, 0 < P_{dry} \le P_{MC} \\ 1.3732 & P_{dry} > P_{MC} \end{cases} \quad (2.15)$$

Grujicic and Bell (2011) proposed relation of shear modulus vs density using a polynomial function as Eq. 2.16. Here, G_{Bulk} (3.7347×10^7 kPa) is the shear modulus of fully compacted dry sand.

$$G(kPa) = \begin{cases} 5.217510^{-14}(\rho - \alpha_0\beta_0\rho_w)^6 & \rho < (1-\alpha_0\beta_0)\rho_{ref} + \alpha_0\beta_0\rho_w \\ (1-\alpha_0\beta_0)G_{Bulk} & \rho \ge (1-\alpha_0\beta_0)\rho_{ref} + \alpha_0\beta_0\rho_w \end{cases} \quad (2.16)$$

In strength model for saturated sand, Grujicic *et al*. (2008) noted that the contribution of water to material strength was neglected because the contribution of water to the shear strength of the sand is very small.

In this paper, the P_{min} failure model is used. The P_{min} failure model allows a maximum value of the hydrodynamic pressure. If the material pressure is below a minimum value of the hydrodynamic pressure, the material instantaneously fails and loses its ability to support any tensile of shear stresses. In addition, considering CU-ARL sand erosion model, the geometrical instantaneous strain is assumed 2.0, based on the study by Grujicic *et al*. (2007).

Table 2.2. Material property of saturated sand (70%) and gravel (30%) (Grujicic and Bell, 2011)

Parameter	Unit	Piece-wise model relations									
Reference density	kg/m^3	2,641.0									
Compaction equation of state											
Density	kg/m^3	2,062	2,090	2,119	2,149	2,179	2,209	2,239	2,269	2,300	2,362
Pressure	GPa	0	0.5651	1.30	2.04	2.77	3.51	4.25	4.99	5.73	7.20
Sound speed	m/s	5,016	5,016	5,016	5,016	5,016	5,016	5,016	5,016	5,016	5,016
MO granular strength model											
Pressure	MPa	0	46.15	92.30	138.5	184.6	230.7	–	–	–	–
Yield stress	MPa	0	27.00	87.26	180.8	307.6	307.6	–	–	–	–
Density	kg/m^3	2,062	2092	2,122	2,152	2,182	2,212	2,242	2,272	2,302	2,362
Shear modulus	GPa	1.70	25.3	25.3	25.3	25.3	25.3	25.3	25.3	25.3	25.3
P_{min} failure model											
Hydro tensile limit	kPa	-80.56									
Erosion											
Geometric strain	–	2.0									

Table 2.3. Material property for saturated sand (85%) and clay (15%) (Grujicic and Bell, 2011)

Parameter	Unit	Piece-wise model relations									
Reference density	kg/m^3	2,641.0									
Compaction equation of state											
Density	kg/m^3	1,993	1,999	2,005	2,010	2,022	2,027	2,033	2,039	2,044	2,101
Pressure	MPa	0	61.45	122.9	184.3	245.8	307.3	368.7	430.2	491.6	$1.27\square 10^3$
Sound speed	m/s	3,555	3,555	3,555	3,555	3,555	3,555	3,555	3,555	3,555	3,555
MO granular strength model											
Pressure	MPa	0	26.15	52.32	78.46	104.6	130.78	156.9	183.1	209.3	–
Yield stress	MPa	0	7.021	22.29	45.83	77.65	117.7	166.1	166.1	166.1	–
Density	kg/m^3	2,092	2,153	2,442	2,493	2,624	2,855	2,878	2,909	2,914	3,049
Shear modulus	MPa	75.21	310.6	407.7	414.0	425.3	434.0	436.0	441.4	441.5	441.5
P_{min} failure model											
Hydro tensile limit	kPa	-67									
Erosion											
Geometric strain	–	2.0									

CHAPTER 3
RESULTS

3.1 Collision Analysis – Cube-type Reef

3.1.1 Seabed composed of saturated sand (70%) and gravel (30%)

Figure 3.1, 3.2, and 3.3 show vertical displacement (D_Y) contours and histories of the cube-type reef for the seabed composed of saturated sand (70%) and gravel (30%), when the installation velocity is 0.2m/s, 0.4m/s, and 0.6m/s, respectively. In all three cases, the settlement of the seabed occurred rapidly after collision, but it became constant in about 0.05 seconds. The gauges from 1 to 4 located at the center of the AR showed rise of the seabed, and the gauges from 5 to 8 located below the AR showed the settlement of the seabed. Moreover, the settlement value was much larger than the rising value, and the closer the gauge was to the AR, the larger the value. The maximum values of settlement were all found on gauge 5, and the values were 0.18cm, 0.23cm, and 0.29cm, respectively. The faster the installation velocity, the greater the settlement, but a very small difference.

Figure 3.4 and 3.5 show vertical displacement (D_Y) contours and histories of the cube-type reef for the seabed composed of saturated sand (70%) and gravel (30%), when the installation velocity is 0.2m/s and the installation angle are 5˚, 10˚, and 15˚, respectively. The maximum values of settlement were all found on gauge 9, and the values were 2.9cm, 4.1cm, and 6.6cm, respectively.

Figure 3.6 and 3.7 show vertical displacement (D_Y) contours and histories of the cube-type reef for the seabed composed of saturated sand

(70%) and gravel (30%), when the installation velocity is 0.4m/s and the installation angle are 5˚, 10˚, and 15˚, respectively. The maximum values of the settlement were all found on gauge 9, and the values were 3.0cm, 4.3cm, and 6.8cm, respectively.

Figure 3.8 and 3.9 show vertical displacement (D_Y) contours and histories of the cube-type reef for the seabed composed of saturated sand (70%) and gravel (30%), when the installation velocity is 0.6m/s and the installation angle are 5˚, 10˚, and 15˚, respectively. The maximum values of the settlement were all found on gauge 9, and the values were 3.2cm, 4.6cm, and 7.0cm, respectively. Regardless of the installation velocity, the larger the installation angle, the greater the initial settlement.

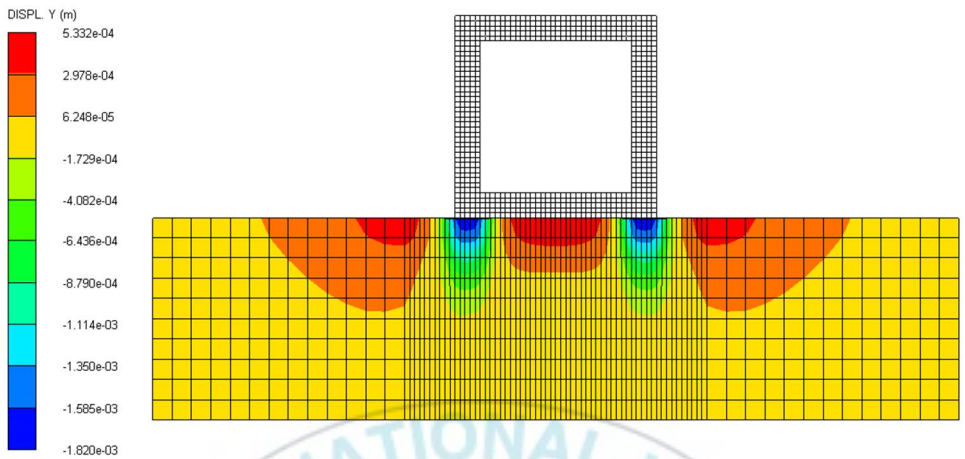

(a) vertical displacement (D_Y) contour

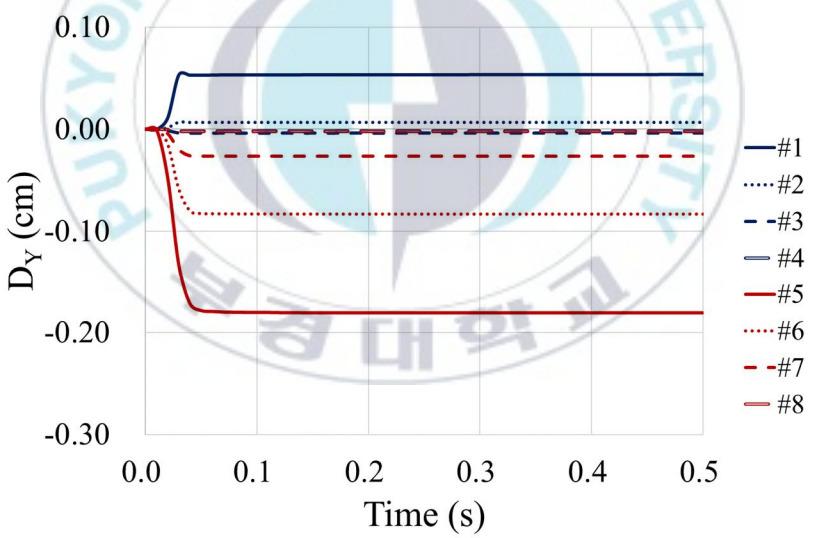

(b) vertical displacement (D_Y) history

Fig. 3.1. Results of the cube-type reef for the seabed composed of saturated sand (70%) and gravel (30%), when the installation velocity is 0.2m/s and the installation angle is 0˚.

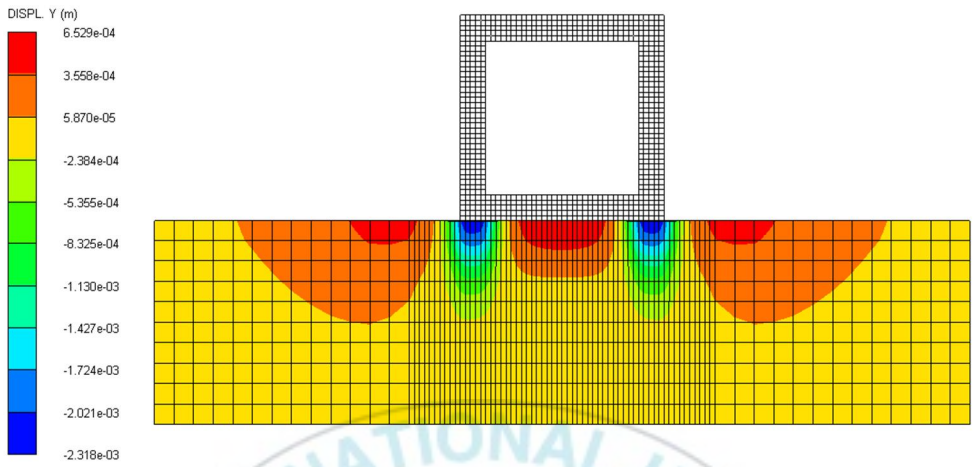

(a) vertical displacement (D_Y) contour

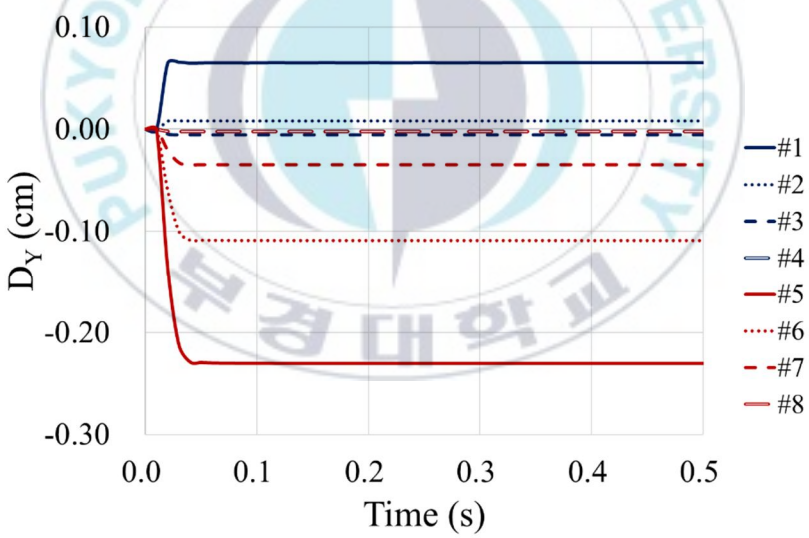

(b) vertical displacement (D_Y) history

Fig. 3.2. Results of the cube-type reef for the seabed composed of saturated sand (70%) and gravel (30%), when the installation velocity is 0.4m/s and the installation angle is 0˚.

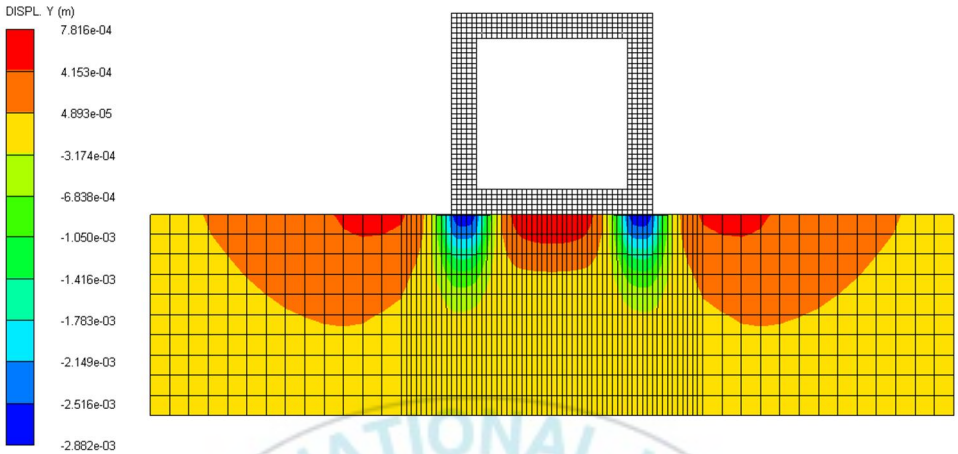

(a) vertical displacement (D_Y) contour

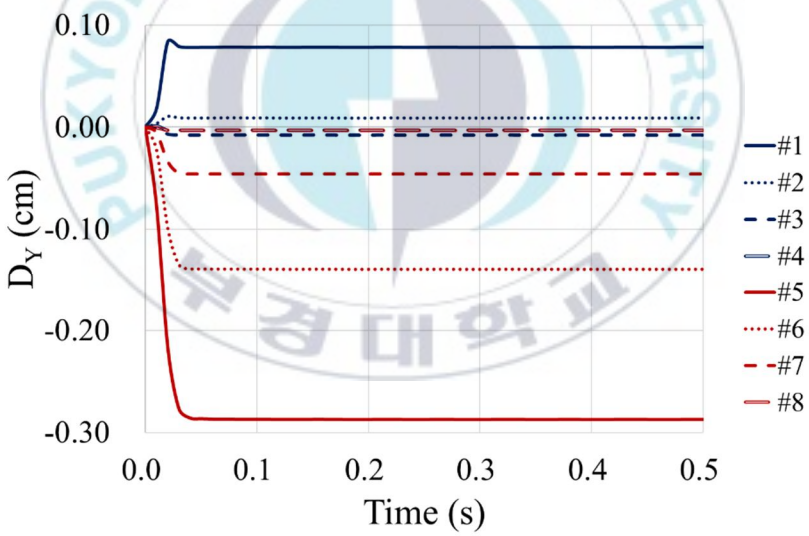

(b) vertical displacement (D_Y) history

Fig. 3.3. Results of the cube-type reef for the seabed composed of saturated sand (70%) and gravel (30%), when the installation velocity is 0.6m/s and the installation angle is 0˚.

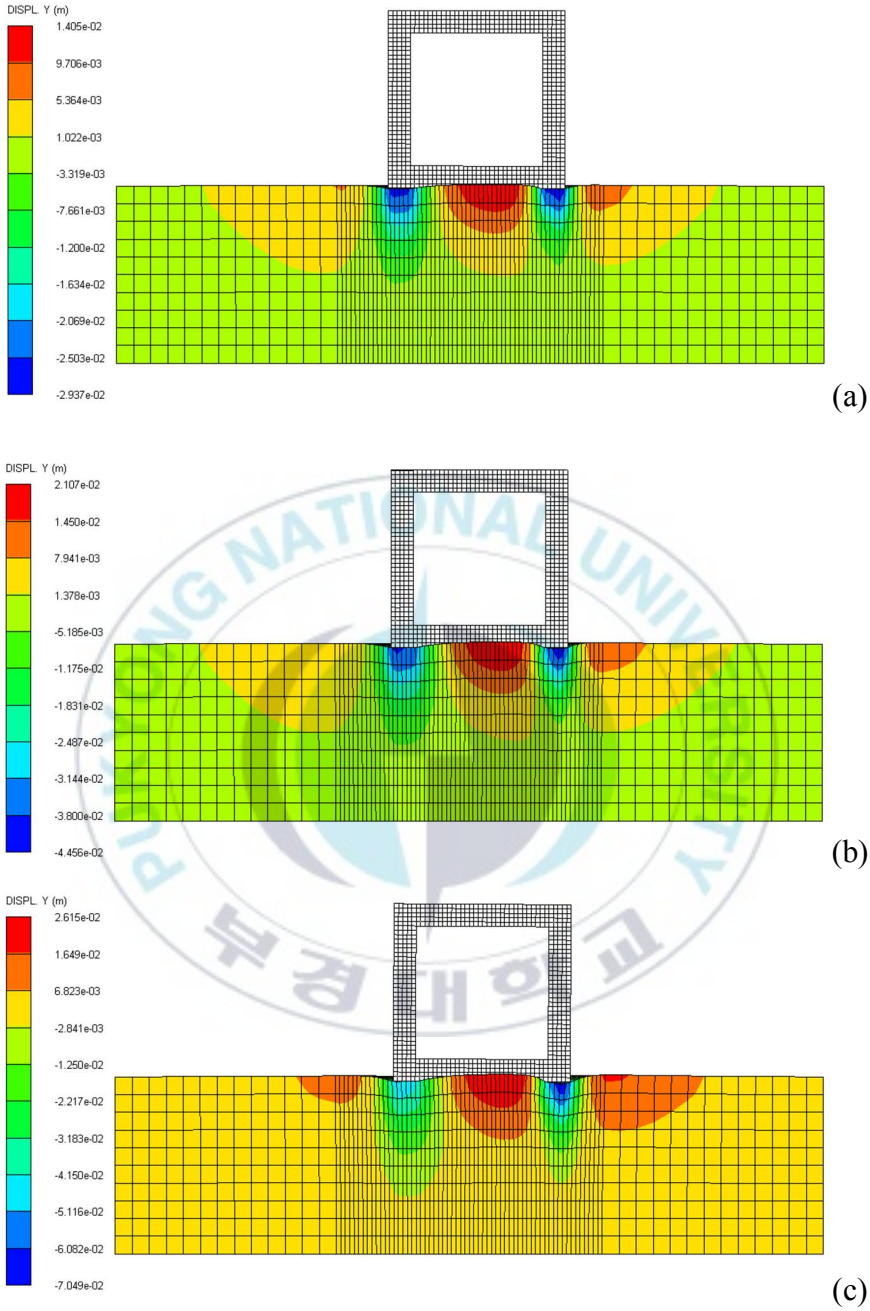

Fig. 3.4. Vertical displacement (D_Y) contours of the cube-type reef for the seabed composed of saturated sand (70%) and gravel (30%), when the installation velocity is 0.2m/s: (a) $\theta = 5^{\circ}$, (b) $\theta = 10^{\circ}$, and (c) $\theta = 15^{\circ}$.

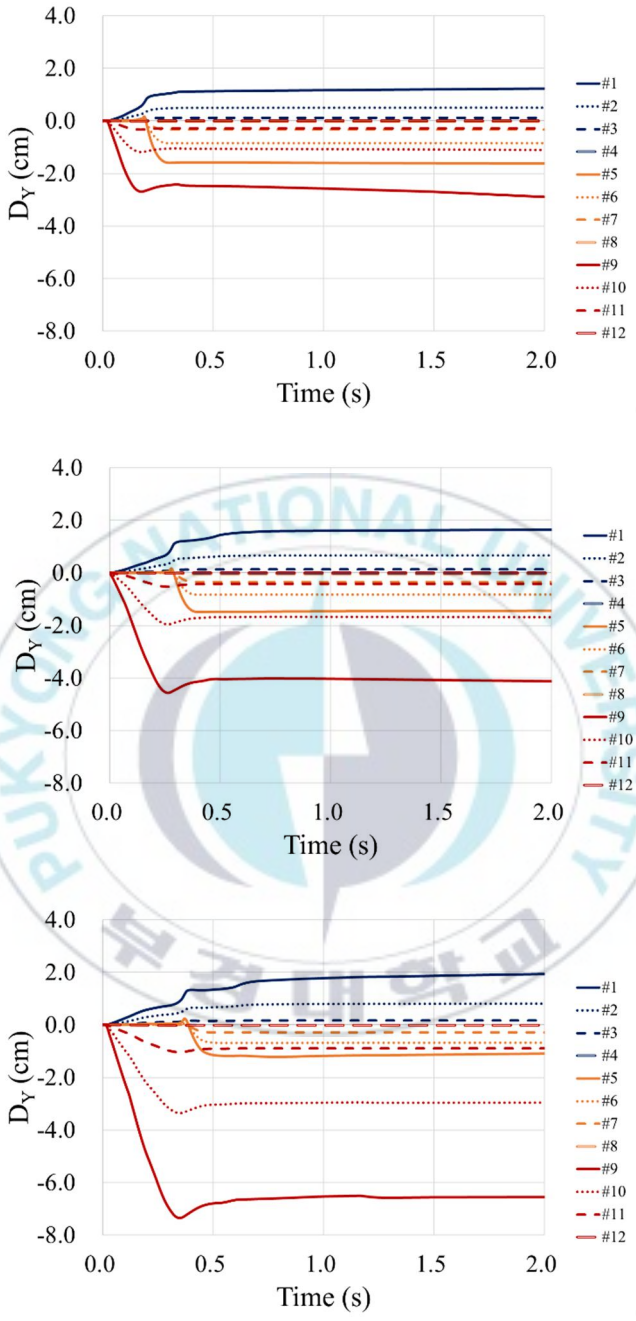

Fig. 3.5. Vertical displacement (D_Y) histories of the cube-type reef for the seabed composed of saturated sand (70%) and gravel (30%), when the installation velocity is 0.2m/s: (a) θ = 5˚, (b) θ = 10˚, and (c) θ = 15˚.

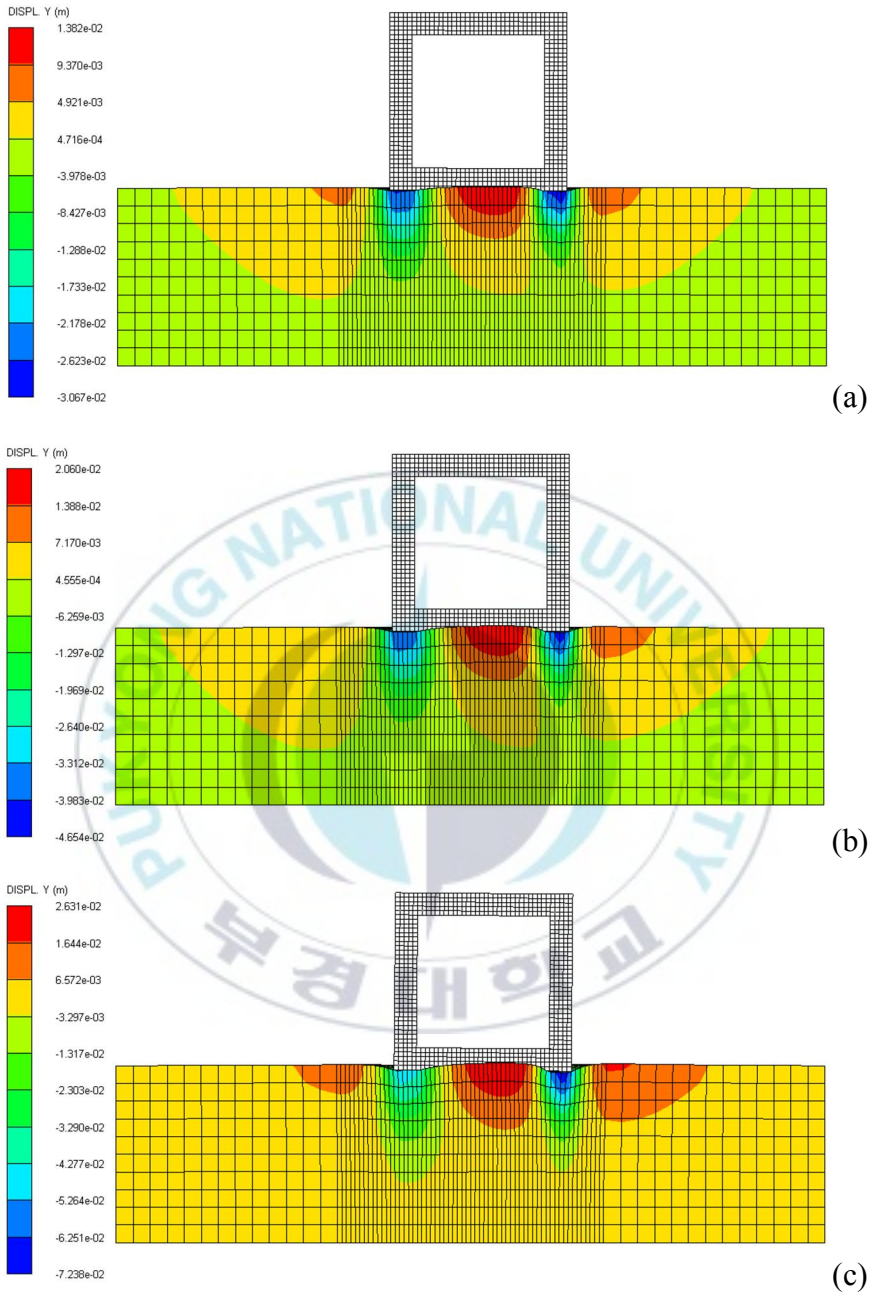

Fig. 3.6. Vertical displacement (D_Y) contours of the cube-type reef for the seabed composed of saturated sand (70%) and gravel (30%), when the installation velocity is 0.4m/s: (a) $\theta = 5^{\circ}$, (b) $\theta = 10^{\circ}$, and (c) $\theta = 15^{\circ}$.

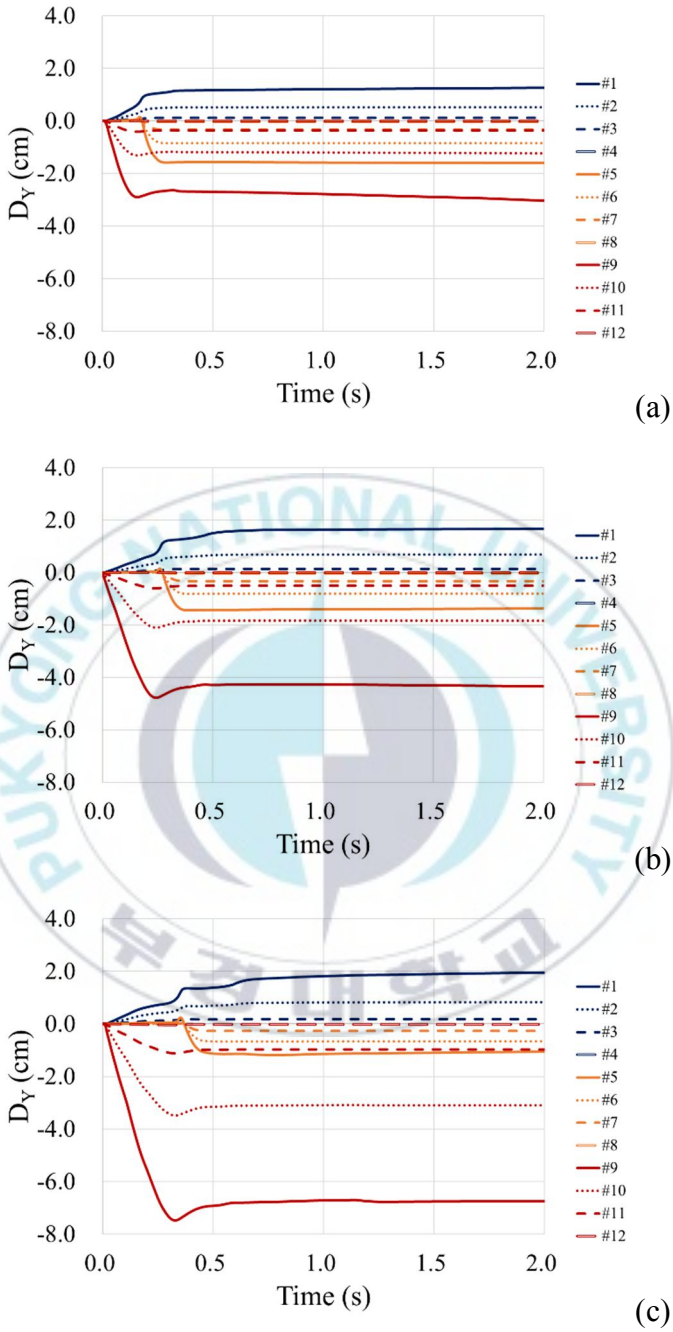

Fig. 3.7. Vertical displacement (D_Y) histories of the cube-type reef for the seabed composed of saturated sand (70%) and gravel (30%), when the installation velocity is 0.4m/s: (a) θ = 5˚, (b) θ = 10˚, and (c) θ = 15˚.

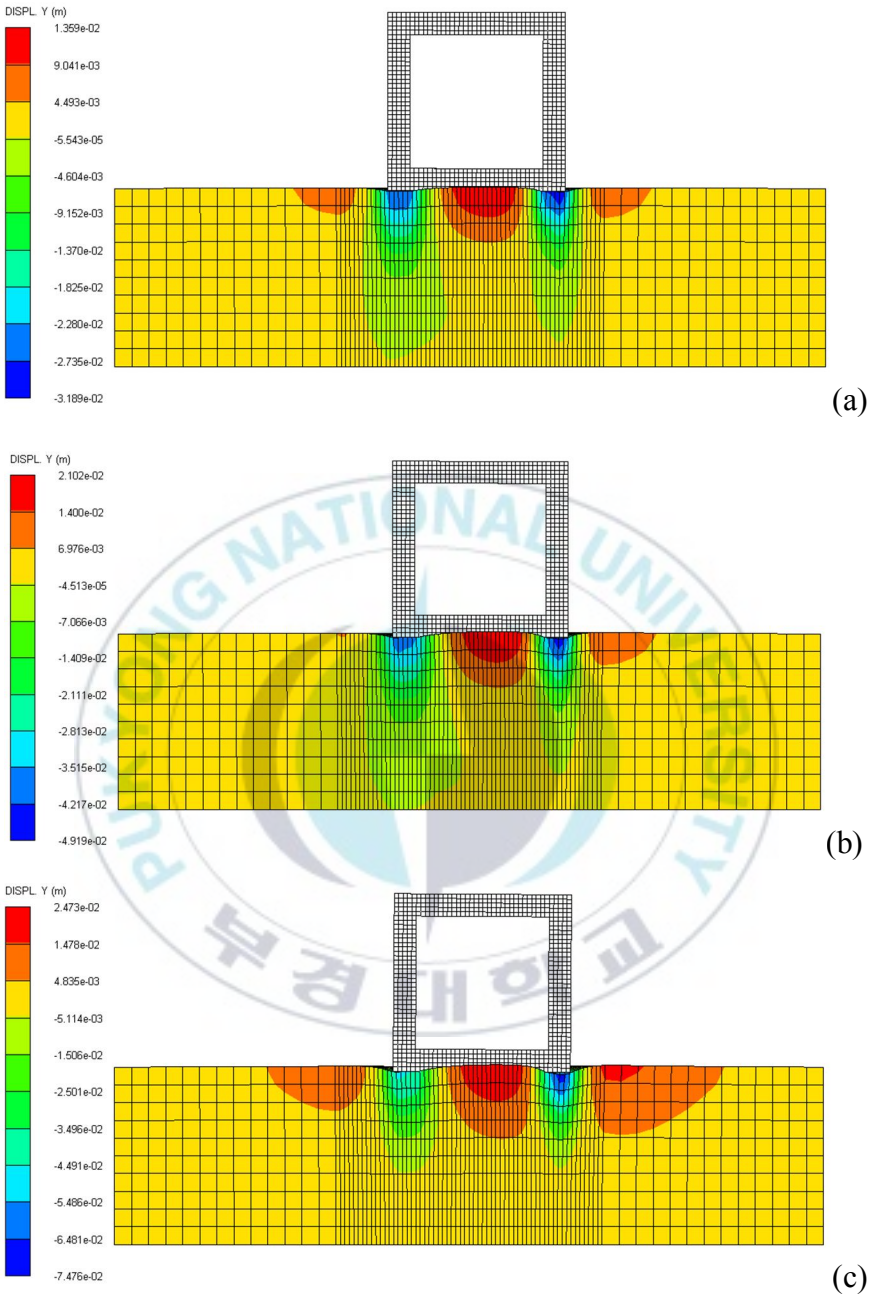

Fig. 3.8. Vertical displacement (D_Y) contours of the cube-type reef for the seabed composed of saturated sand (70%) and gravel (30%), when the installation velocity is 0.6m/s: (a) $\theta = 5^{\circ}$, (b) $\theta = 10^{\circ}$, and (c) $\theta = 15^{\circ}$.

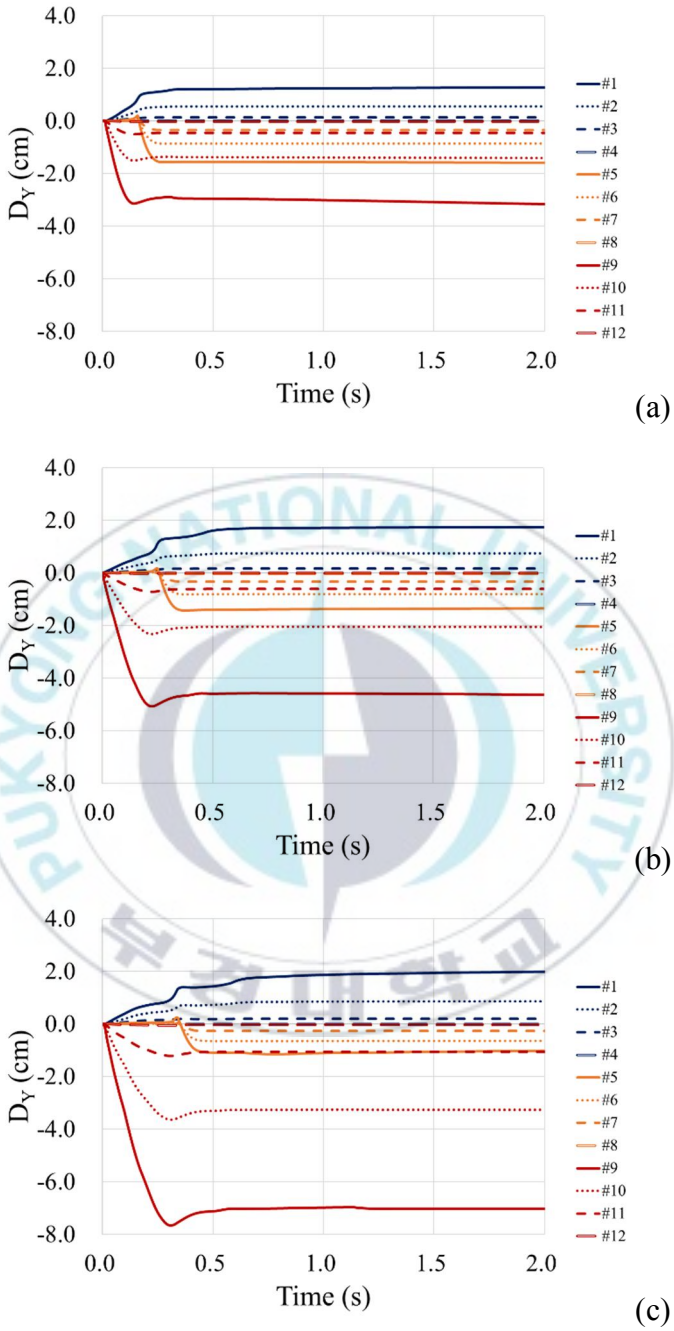

Fig. 3.9. Vertical displacement (D_Y) histories of the cube-type reef for the seabed composed of saturated sand (70%) and gravel (30%), when the installation velocity is 0.6m/s: (a) θ = 5˚, (b) θ = 10˚, and (c) θ = 15˚.

3.1.2 Seabed composed of saturated sand (85%) and clay (15%)

Figure 3.10, 3.11, and 3.12 show vertical displacement (D_Y) contours and histories of the cube-type reef for the seabed composed of saturated sand (85%) and clay (15%), when the installation velocity is 0.2m/s, 0.4m/s, and 0.6m/s, respectively. In all three cases, the settlement of the seabed gradually progressed after the collision compared with the seabed composed of saturated sand (70%) and gravel (30%), and showed that reached the steady state after one second. Like the seabed composed of saturated sand (70%) and gravel (30%), the gauges from 1 to 4 located at the center of the AR showed rise of the seabed, and the gauges from 5 to 8 located below the AR showed the settlement of the seabed. Moreover, the settlement value was much larger than the rising value, and the closer the gauge was to the AR, the larger the value. The maximum values of the settlement were all found on gauge 5, and the values were 39.3cm, 39.4cm, and 39.6cm, respectively. The results also show that the faster the installation velocity, the greater the settlement, but the difference is small.

Figure 3.13 and 3.14 show vertical displacement (D_Y) contours and histories of the cube-type reef for the seabed composed of saturated sand (70%) and gravel (30%), when the installation velocity is 0.2m/s and the installation angle are 5˚, 10˚, and 15˚, respectively. The maximum values of the settlement were all found on gauge 9, and the values were 45.9cm, 47.9cm, and 53.0cm, respectively.

Figure 3.15 and 3.16 show vertical displacement (D_Y) contours and histories of the cube-type reef for the seabed composed of saturated sand (70%) and gravel (30%), when the installation velocity is 0.4m/s and the installation angle are 5˚, 10˚, and 15˚, respectively. The maximum values of

the settlement were all found on gauge 9, and the values were 46.1cm, 48.2cm, and 53.3cm, respectively.

Figure 3.17 and 3.18 show vertical displacement (D_Y) contours and histories of the cube-type reef for the seabed composed of saturated sand (70%) and gravel (30%), when the installation velocity is 0.6m/s and the installation angle are 5˚, 10˚, and 15˚, respectively. The maximum values of the settlement were all found on gauge 9, and the values were 46.3cm, 48.2cm, and 53.4cm, respectively. Regardless of the installation velocity, the larger the installation angle, the greater the initial settlement.

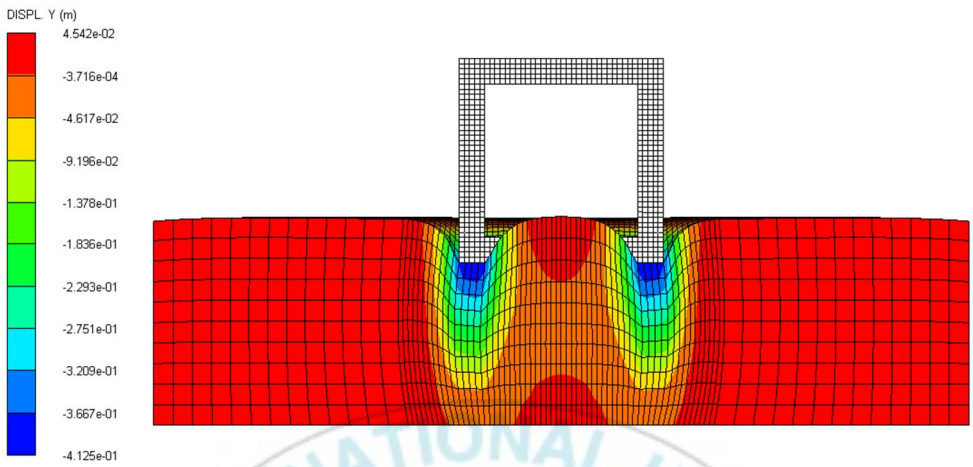

(a) vertical displacement (D_Y) contour

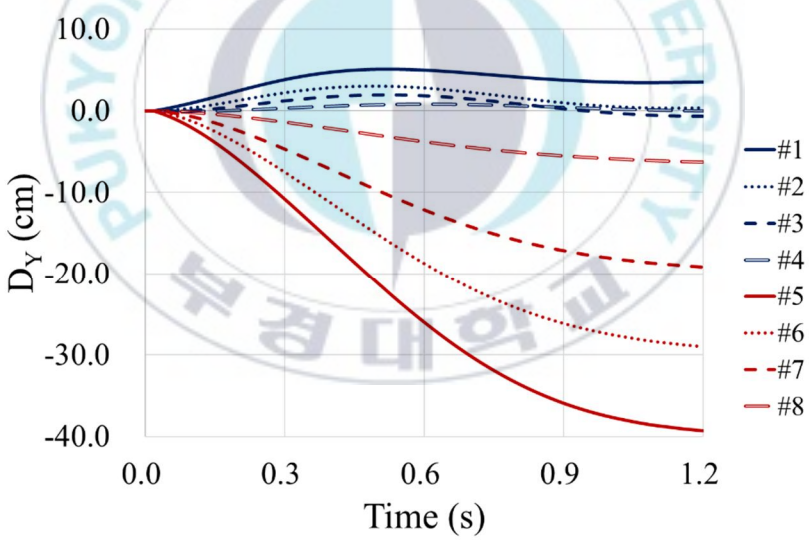

(b) vertical displacement (D_Y) history

Fig. 3.10. Results of the cube-type reef for the seabed composed of saturated sand (85%) and clay (15%), when the installation velocity is 0.2m/s and the installation angle is 0˚.

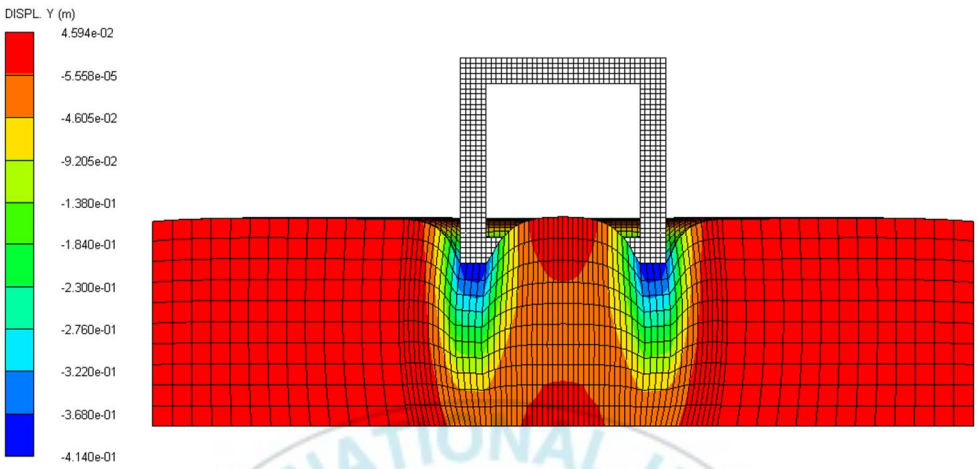

(a) vertical displacement (D_Y) contour

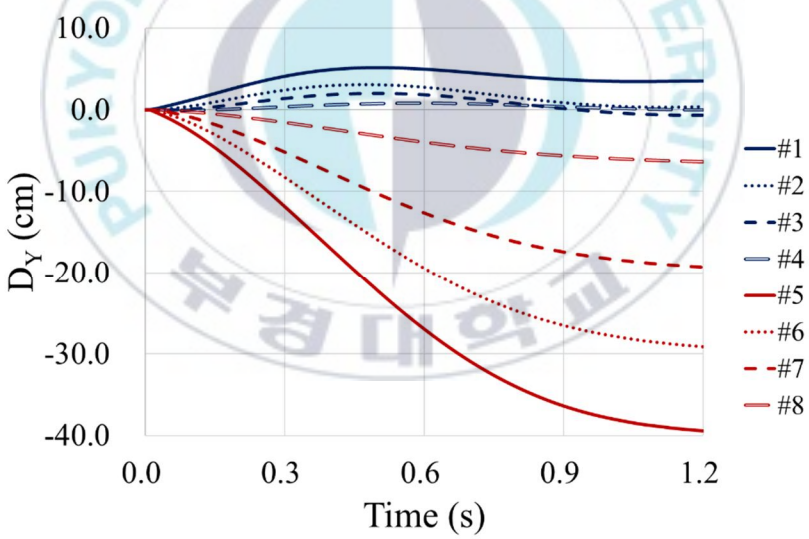

(b) vertical displacement (D_Y) history

Fig. 3.11. Results of the cube-type reef for the seabed composed of saturated sand (85%) and clay (15%), when the installation velocity is 0.4m/s and the installation angle is 0˚.

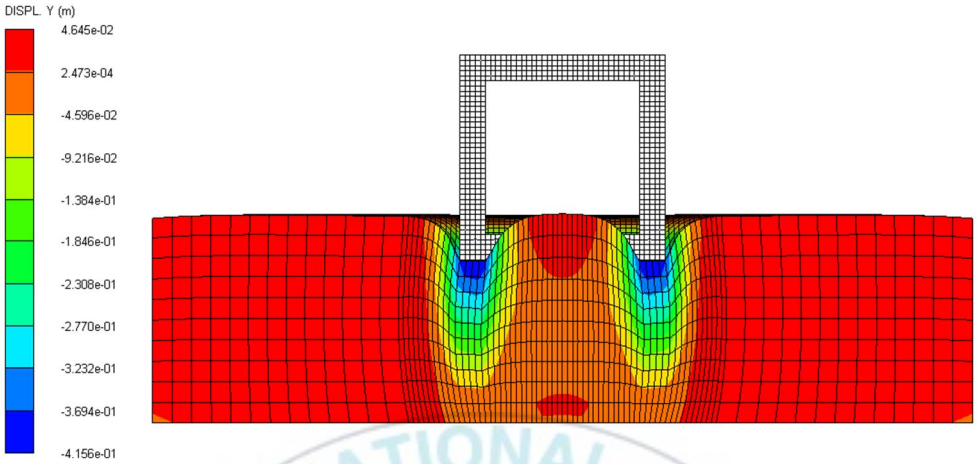

(a) vertical displacement (D_Y) contour

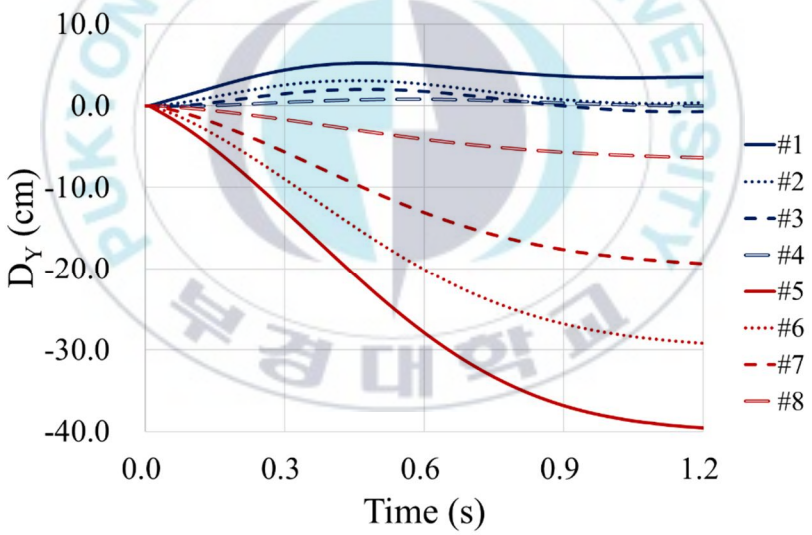

(b) vertical displacement (D_Y) history

Fig. 3.12. Results of the cube-type reef for the seabed composed of saturated sand (85%) and clay (15%), when the installation velocity is 0.6m/s and the installation angle is 0˚.

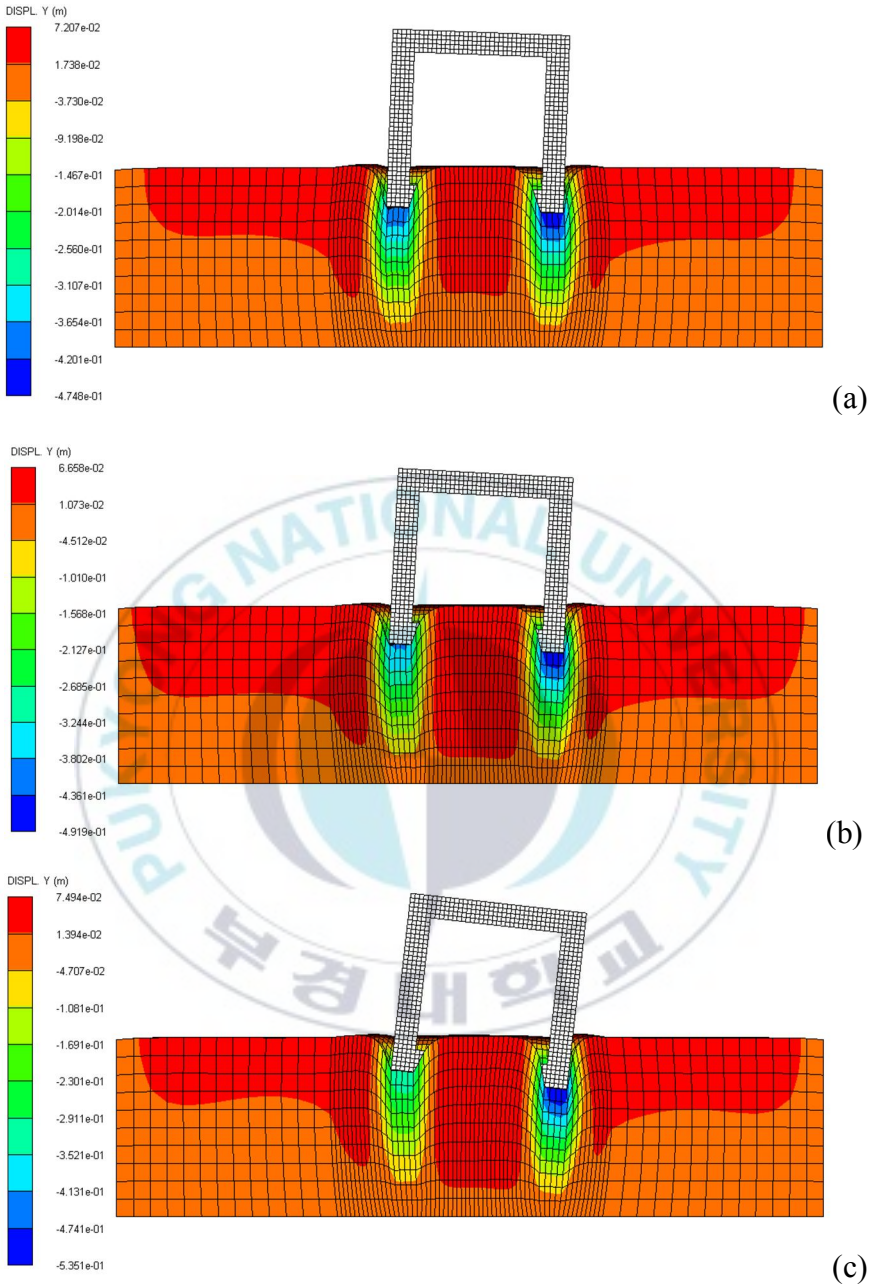

Fig. 3.13. Vertical displacement (D_Y) contours of the cube-type reef for the seabed composed of saturated sand (85%) and clay (15%), when the installation velocity is 0.2m/s: (a) $\theta = 5^{\circ}$, (b) $\theta = 10^{\circ}$, and (c) $\theta = 15^{\circ}$.

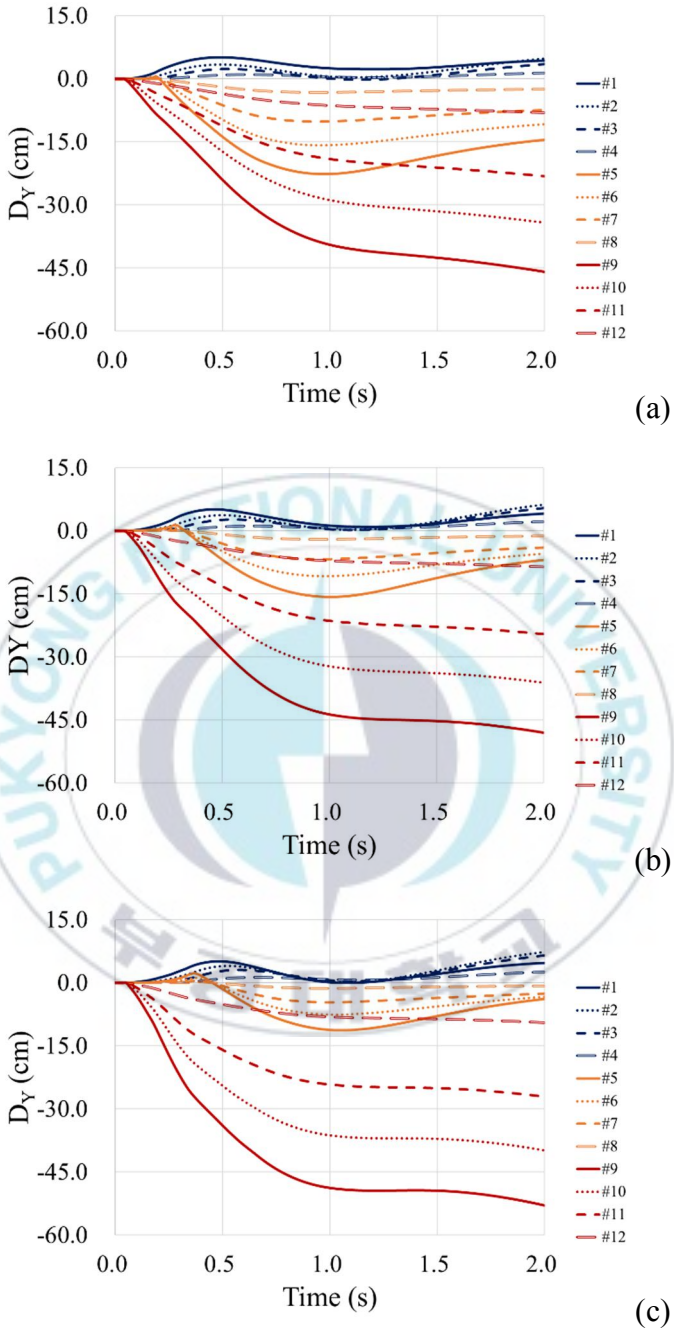

Fig. 3.14. Vertical displacement (D_Y) histories of the cube-type reef for the seabed composed of saturated sand (85%) and clay (15%), when the installation velocity is 0.2m/s: (a) θ = 5˚, (b) θ = 10˚, and (c) θ = 15˚.

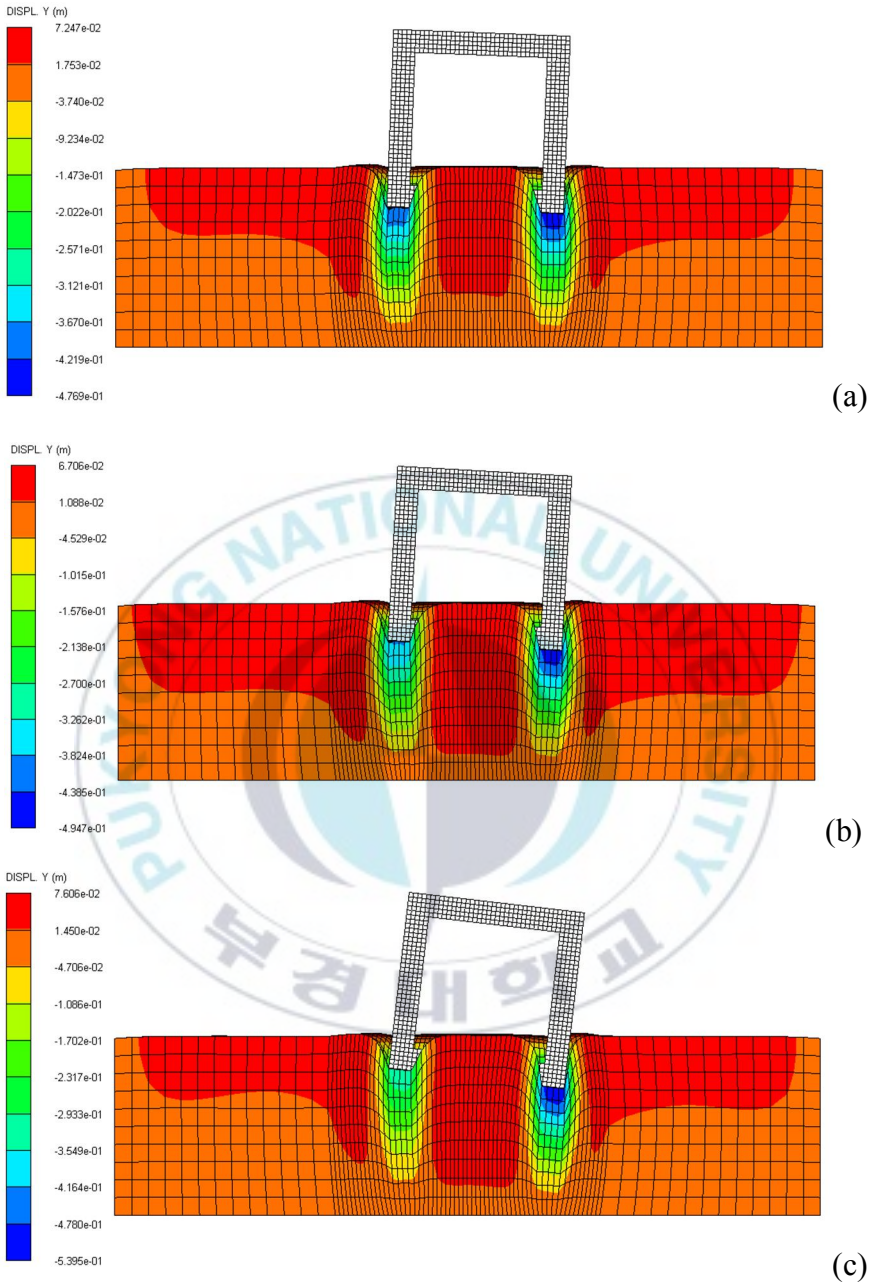

Fig. 3.15. Vertical displacement (D_Y) contours of the cube-type reef for the seabed composed of saturated sand (85%) and clay (15%), when the installation velocity is 0.4m/s: (a) $\theta = 5^{\circ}$, (b) $\theta = 10^{\circ}$, and (c) $\theta = 15^{\circ}$.

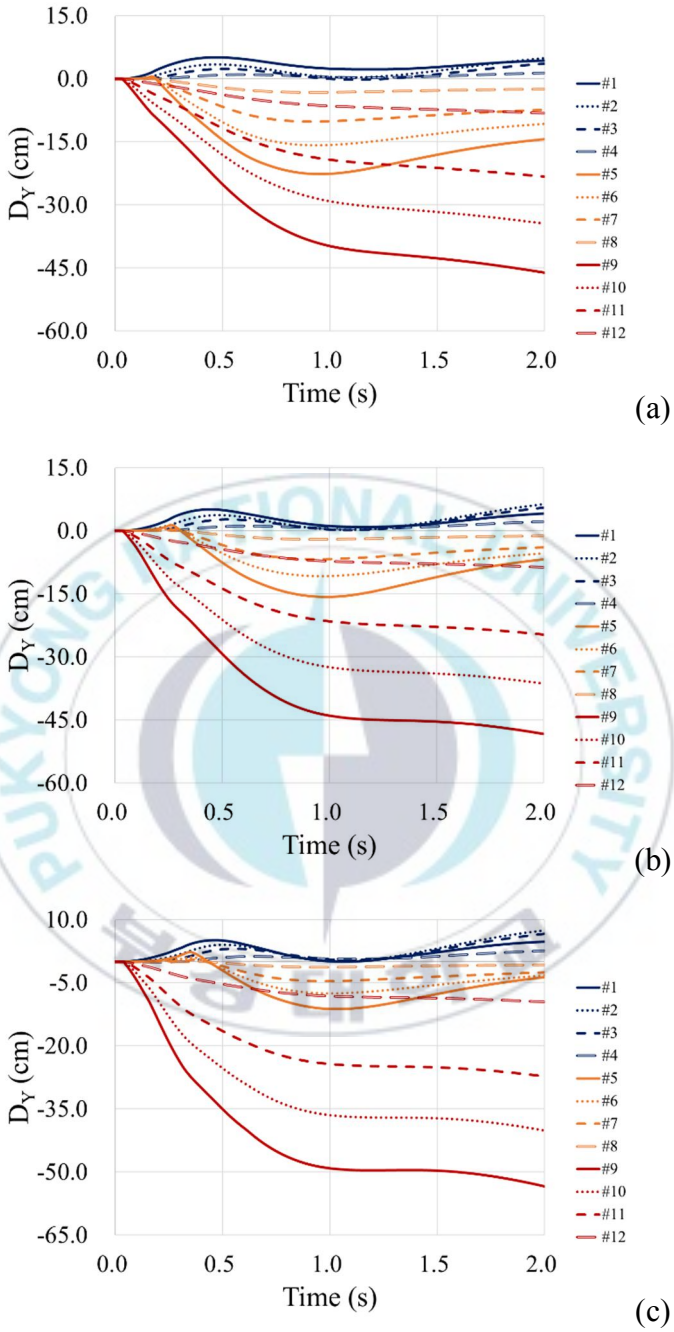

Fig. 3.16. Vertical displacement (D_Y) histories of the cube-type reef for the seabed composed of saturated sand (85%) and clay (15%), when the installation velocity is 0.4m/s: (a) $\theta = 5^{\circ}$, (b) $\theta = 10^{\circ}$, and (c) $\theta = 15^{\circ}$.

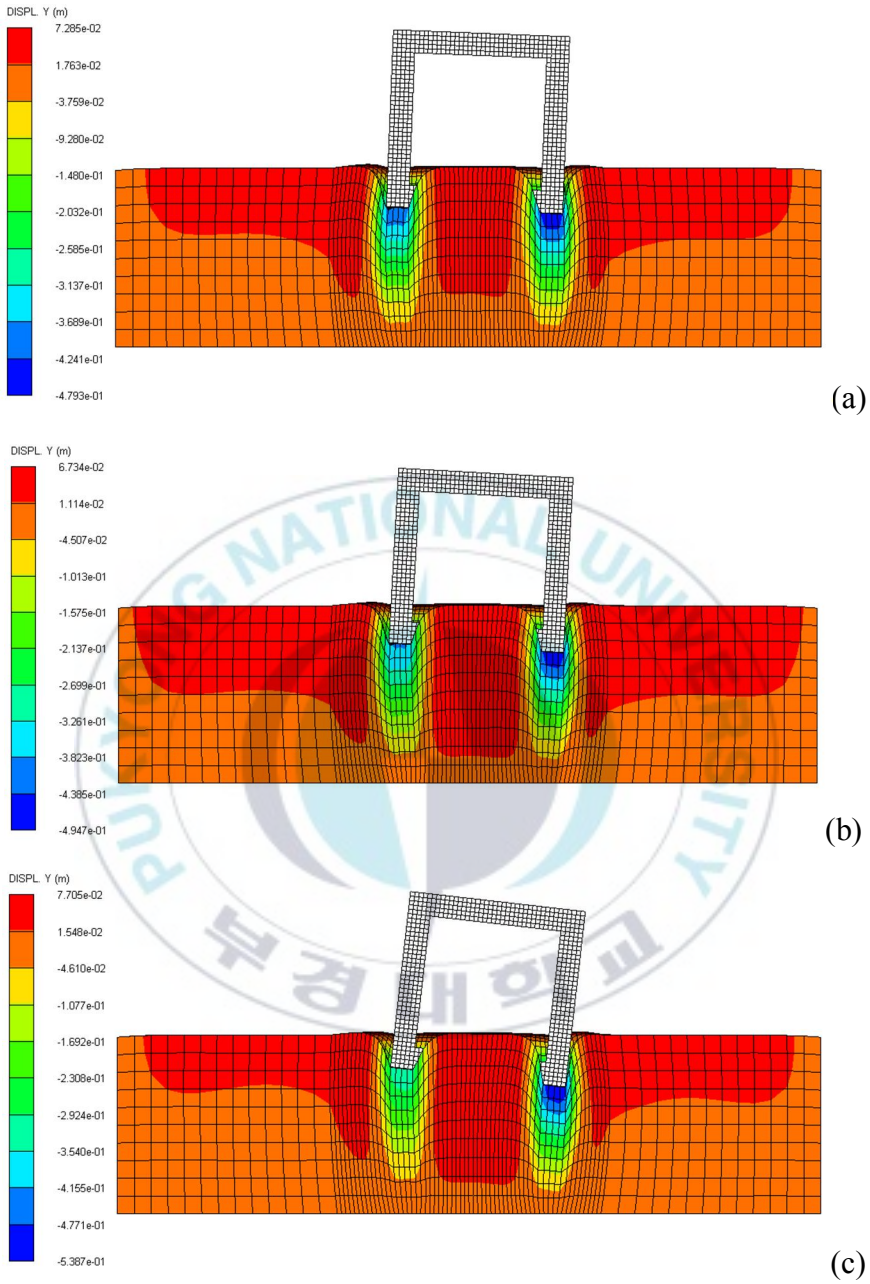

Fig. 3.17. Vertical displacement (D_Y) contours of the cube-type reef for the seabed composed of saturated sand (85%) and clay (15%), when the installation velocity is 0.6m/s: (a) $\theta = 5^{\circ}$, (b) $\theta = 10^{\circ}$, and (c) $\theta = 15^{\circ}$.

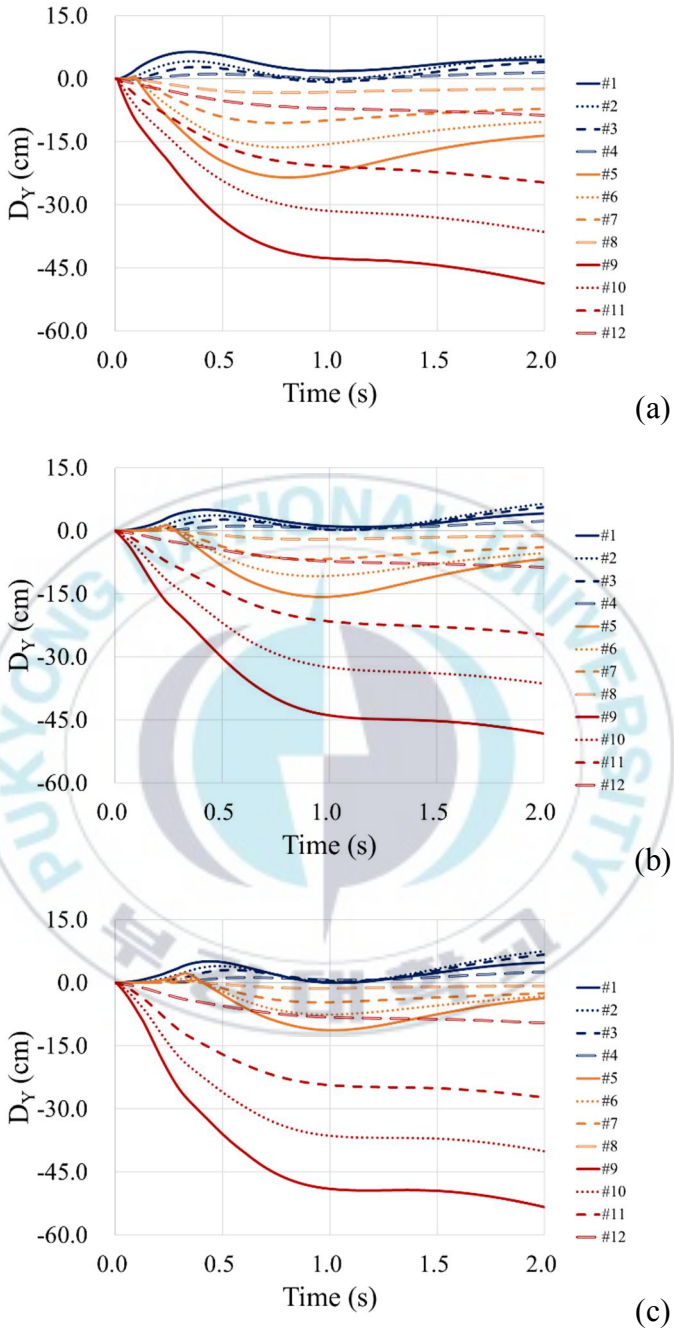

Fig. 3.18. Vertical displacement (D_Y) histories of the cube-type reef for the seabed composed of saturated sand (85%) and clay (15%), when the installation velocity is 0.6m/s: (a) θ = 5˚, (b) θ = 10˚, and (c) θ = 15˚.

3.2 Collision Analysis – Half-ball type Reef

3.2.1 Seabed composed of saturated sand (70%) and gravel (30%)

Figure 3.19, 3.20, and 3.21 show vertical displacement (D_Y) contours and histories of the half-ball type reef for the seabed composed of saturated sand (70%) and gravel (30%), when the installation velocity is 0.2m/s, 0.4m/s, and 0.6m/s, respectively. In all three cases, the settlement of the seabed occurred rapidly after collision, and loosely after 0.5 second. Similar to the case where the result is the cube-type reef, but the value is not constant and has a slight slope. All gauges from 2 to 8, except gauge 1, showed the settlement of the seabed. The maximum values of the settlement were all found on gauge 5, and the values were 0.35cm, 0.37cm, and 0.44cm, respectively. The value is larger than the cube-type reef, but it is the same that the faster the installation velocity, the larger the settlement.

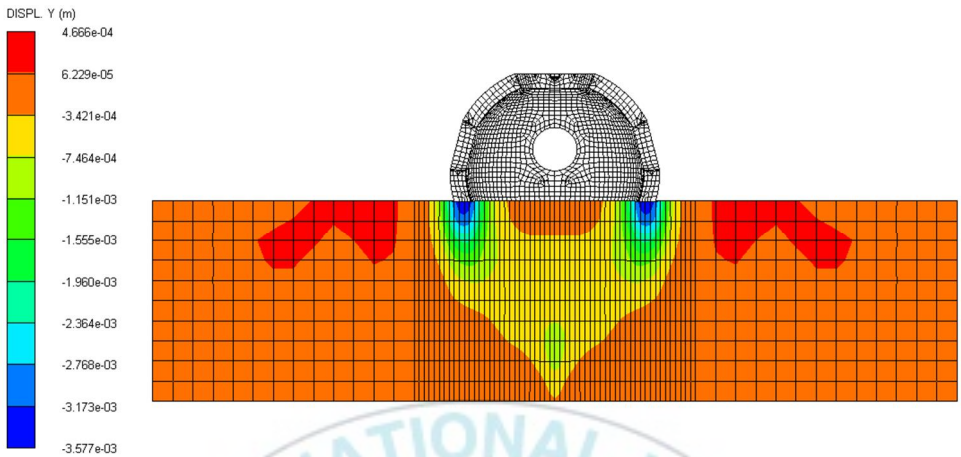

(a) vertical displacement (D_Y) contour

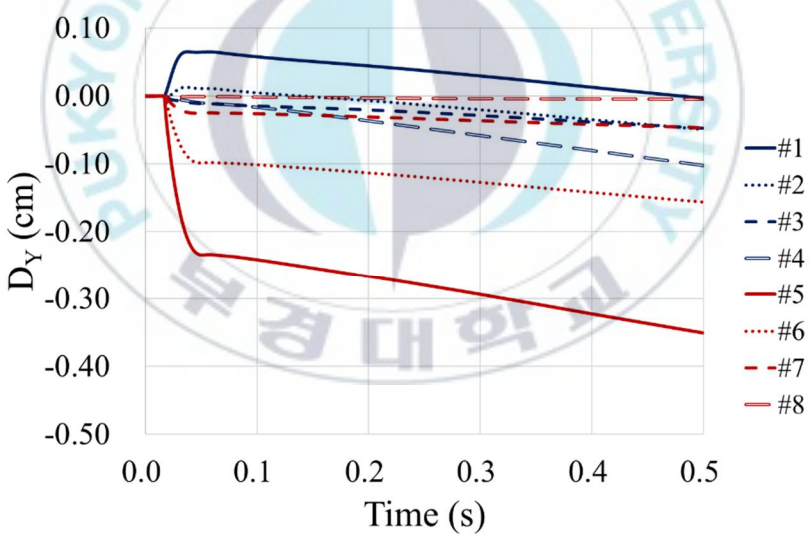

(b) vertical displacement (D_Y) history

Fig. 3.19. Results of the half-ball type reef for the seabed composed of saturated sand (70%) and gravel (30%), when the installation velocity is 0.2m/s.

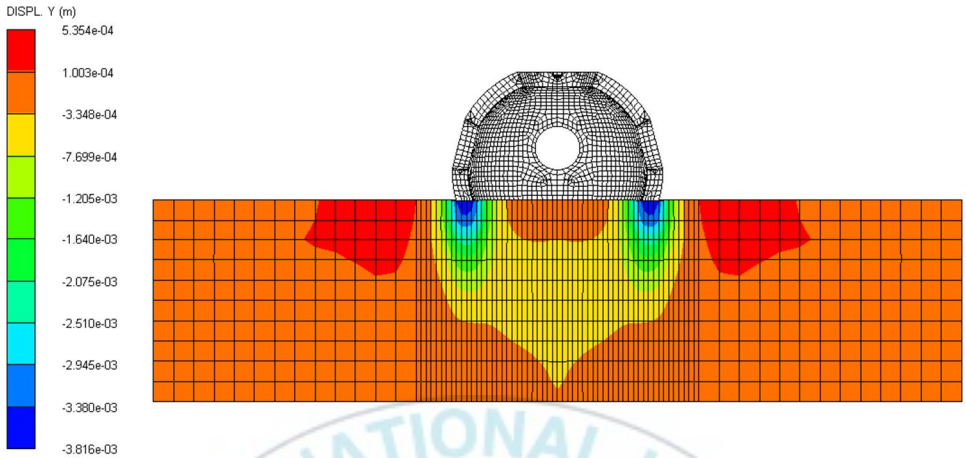

(a) vertical displacement (D_Y) contour

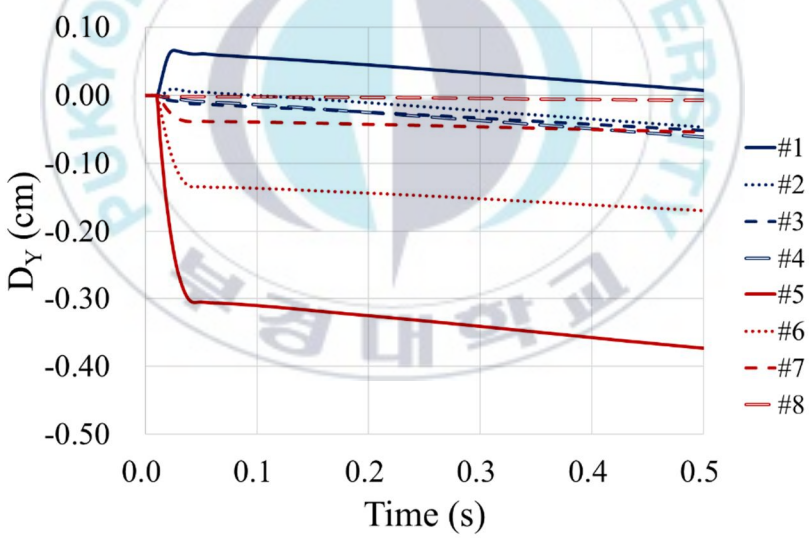

(b) vertical displacement (D_Y) history

Fig. 3.20. Results of the half-ball type reef for the seabed composed of saturated sand (70%) and gravel (30%), when the installation velocity is 0.4m/s.

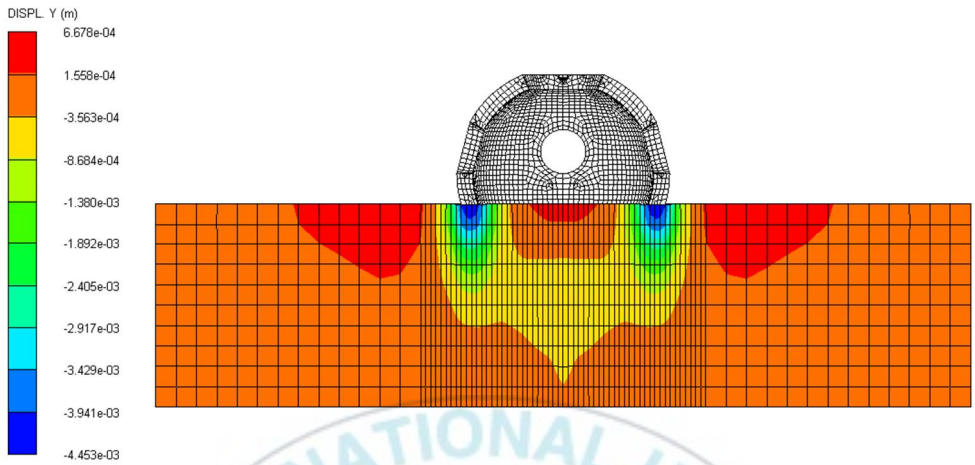

(a) vertical displacement (D_Y) contour

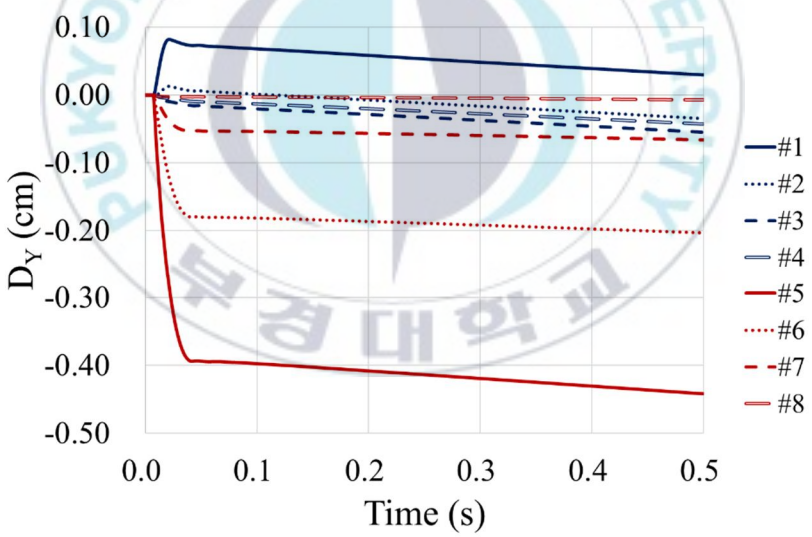

(b) vertical displacement (D_Y) history

Fig. 3.21. Results of the half-ball type reef for the seabed composed of saturated sand (70%) and gravel (30%), when the installation velocity is 0.6m/s.

3.2.2 Seabed composed of saturated sand (85%) and clay (15%)

Figure 3.22, 3.23, and 3.24 show vertical displacement (D_Y) contours and histories of the half-ball type reef for the seabed composed of saturated sand (85%) and clay (15%), when the installation velocity is 0.2m/s, 0.4m/s, and 0.6m/s, respectively. In all three cases, the settlement of the seabed gradually progressed after the collision, and showed that reached the steady stated after one second. The gauges from 1 to 4 located at the center of the AR showed rise of the seabed, and the gauges from 5 to 8 located below the AR showed the settlement of the seabed. However, the gauges from 1 to 4 tend to the settlement after about 0.7 seconds. The maximum values of the settlement were all found on gauge 5, and the values were 39.2cm, 39.3cm, and 39.5cm, respectively. The results are similar to cube-type reef. And it also shows that the faster the installation velocity, the greater the settlement, but the difference is small.

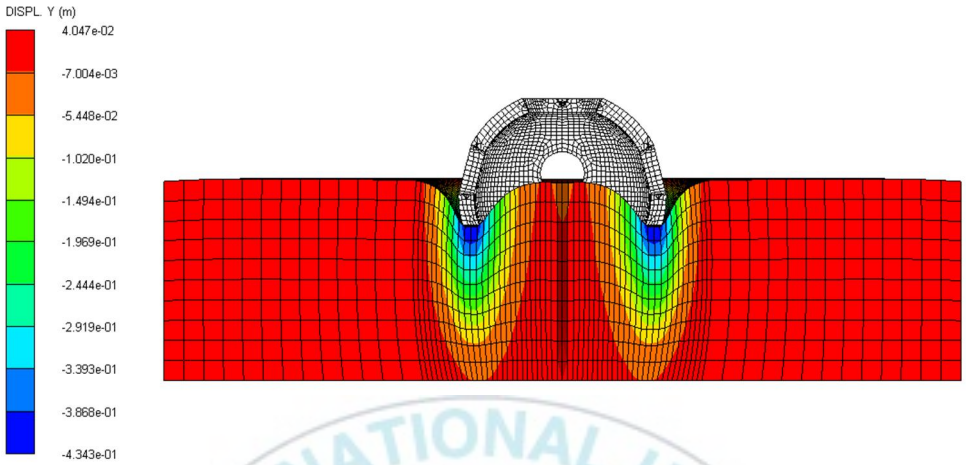

(a) vertical displacement (D_Y) contour

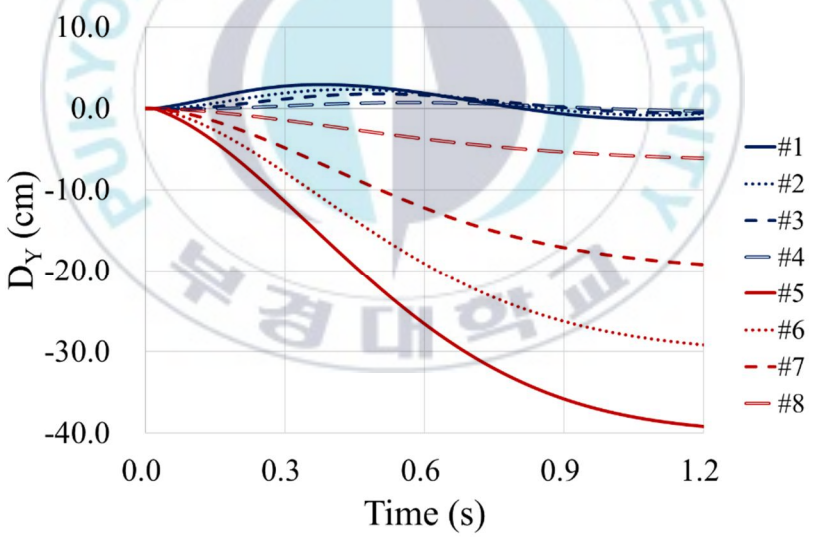

(b) vertical displacement (D_Y) history

Fig. 3.22. Results of the half-ball type reef for the seabed composed of saturated sand (85%) and clay (15%), when the installation velocity is 0.2m/s.

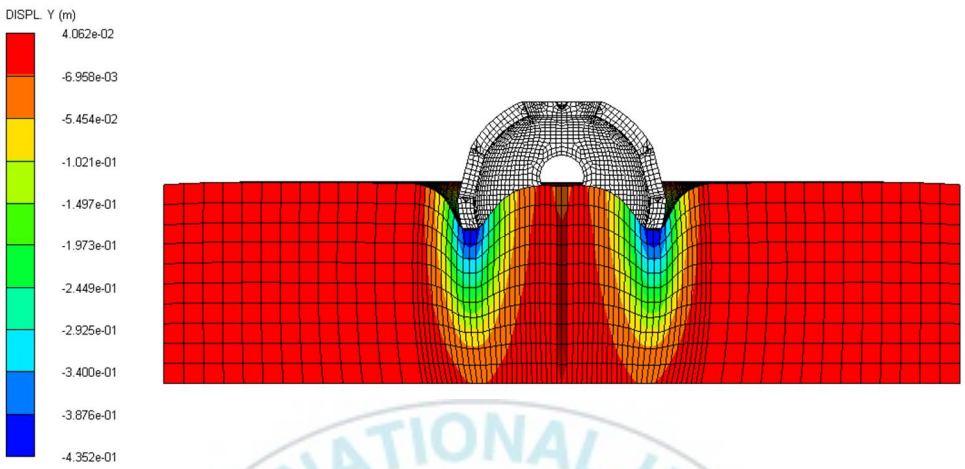

(a) vertical displacement (D_Y) contour

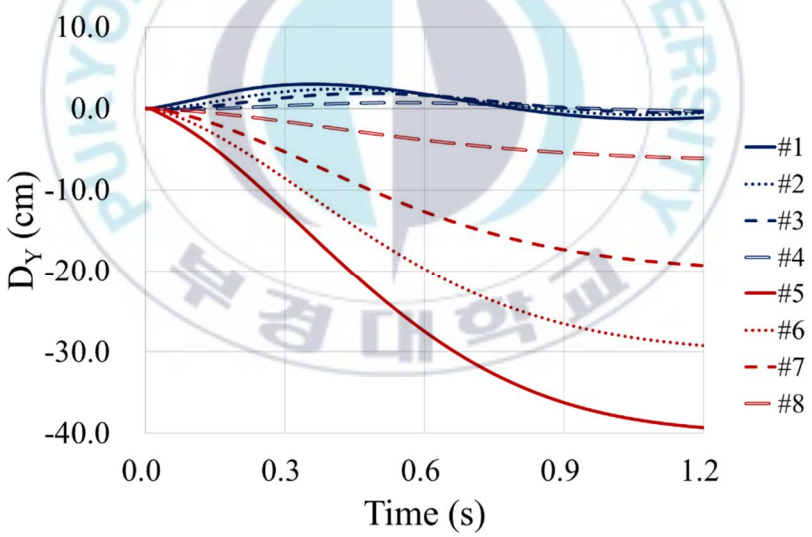

(b) vertical displacement (D_Y) history

Fig. 3.23. Results of the half-ball type reef for the seabed composed of saturated sand (85%) and clay (15%), when the installation velocity is 0.4m/s.

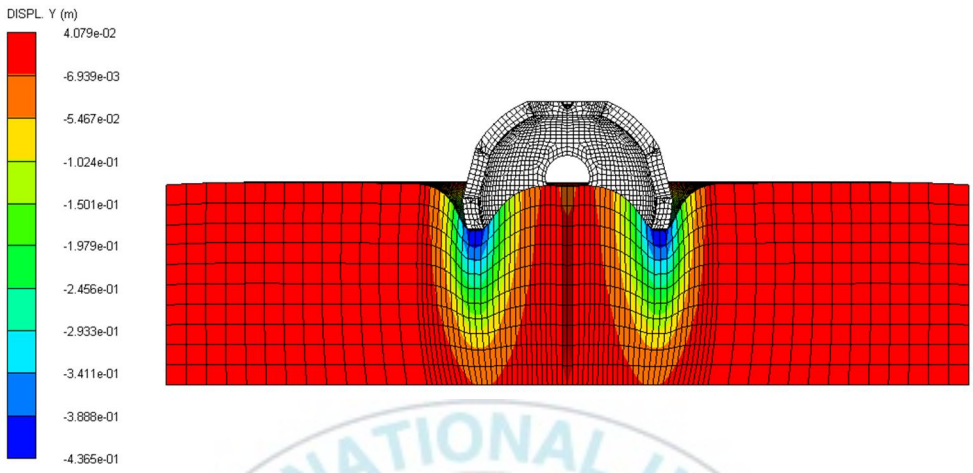

(a) vertical displacement (D_Y) contour

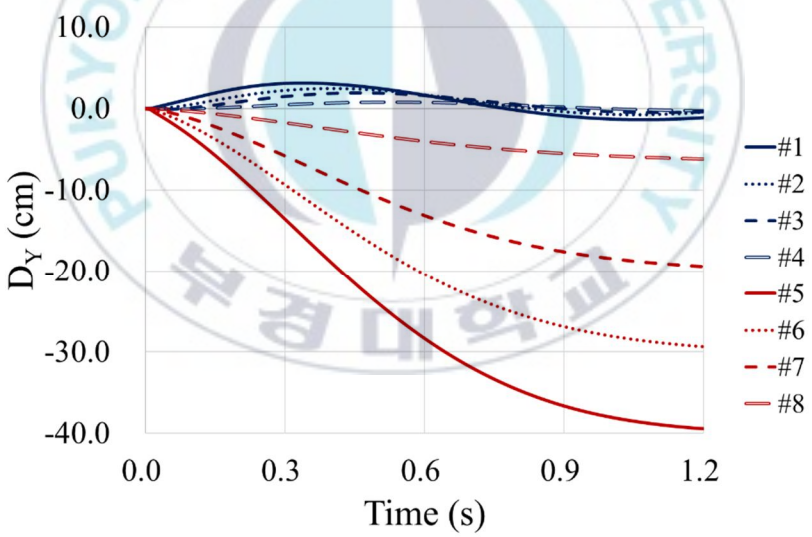

(b) vertical displacement (D_Y) history

Fig. 3.24. Results of the half-ball type reef for the seabed composed of saturated sand (85%) and clay (15%), when the installation velocity is 0.6m/s.

CHAPTER 4
DISSCUSSIONS

Figure 4.1 and 4.2 show vertical displacement (D_Y) history at gauge 5. In all four graphs, the initial settlement tends to increase as the installation velocity increases, but the difference is insignificant. In saturated sand (70%) and gravel (30%) sand soil, the results of the half-ball type reef showed larger values than those of the cube-type reef and the settlements were constant in the cube-type, whereas slightly increased in the half-ball type reef. It is estimated that area where the half-ball reef touches the bottom of the seabed is smaller than the cube-type reef and the weight is smaller. In other words, it seems to be due to that the weight per the bottom dimensions of the half-ball type reef is large. In saturated sand (85%) and clay (15%) sand soil, the settlements were about 39cm regardless of the type of the AR. These results are more than a quarter of the height of the AR.

The effective usable volume is defined as the volume including the space occupied by the AR in the water and the thickness of the member of the AR (Yoon *et al*., 2016). Therefore, the effective usable volume decreases owing to the settlement of the seabed as shown in fig. 4.3. Thus, in this study, is carried out the estimation on the reduction rate of the effective usable volume for the settlement value. The reduction rate of the effective volume for each case is as follows. When it is the cube-type reef, the reduction of the effective volume for the seabed composed of saturated sand (70%) and gravel (30%) is 0.09% (installation velocity is 0.2m/s), 0.12% (installation velocity is 0.4m/s), and 0.15% (installation velocity is 0.6m/s). The reduction rate of the effective volume for the seabed composed of saturated sand (85%) and clay (15%) is 19.65% (installation velocity is 0.2m/s), 19.70% (installation

velocity is 0.4m/s), and 19.80% (installation velocity is 0.6m/s). When it is the half-ball type reef, the reduction rate of the effective volume for the seabed composed of saturated sand (70%) and gravel (30%) is 0.37% (installation velocity is 0.2m/s), 0.39% (installation velocity is 0.4m/s), and 0.46% (installation velocity is 0.6m/s). The reduction rate of the effective volume for the seabed composed of saturated sand (85%) and clay (15%) is 41.03% (installation velocity is 0.2m/s), 41.13% (installation velocity is 0.4m/s), and 41.34% (installation velocity is 0.6m/s). These results are shown in Fig. 4.4. From these results, it can be seen that the reduction of effective usable volume in saturated sand (85%) and clay (15%) seabed is considerable.

The reduction rate of the effective volume considering installation angle cases are as follows. When installation velocity is 0.2m/s, the reduction of the effective volume for the seabed composed of saturated sand (70%) and gravel (30%) is 1.13% (installation angle is 5˚), 1.38% (installation angle is 10˚), and 1.93% (installation angle is 15˚). When installation velocity is 0.4m/s, the reduction rate of the effective is 1.15% (installation angle is 5˚), 1.42% (installation angle is 10˚), and 1.98% (installation angle is 15˚). When installation velocity is 0.6m/s, the reduction rate of the effective is 1.20% (installation angle is 5˚), 1.48% (installation angle is 10˚), and 2.00% (installation angle is 15˚). When installation velocity is 0.2m/s, the reduction of the effective volume for the seabed composed of saturated sand (85%) and clay (15%) is 15.1% (installation angle is 5˚), 13.70% (installation angle is 10˚), and 14.20% (installation angle is 15˚). When installation velocity is 0.4m/s, the reduction rate of the effective is 15.13% (installation angle is 5˚), 13.75% (installation angle is 10˚), and 14.25% (installation angle is 15˚). When installation velocity is 0.6m/s, the reduction rate of the effective is 15.13% (installation angle is 5˚), 13.73% (installation angle is 10˚), and 14.25%

(installation angle is 15˚). These results are shown in Fig. 4.5. From these results, it can be seen that as the installation angle increases, the maximum initial settlement increases, but the reduction rate of effective usable volume tends to decrease in the seabed composed of saturated sand (85%) and clay (15%).

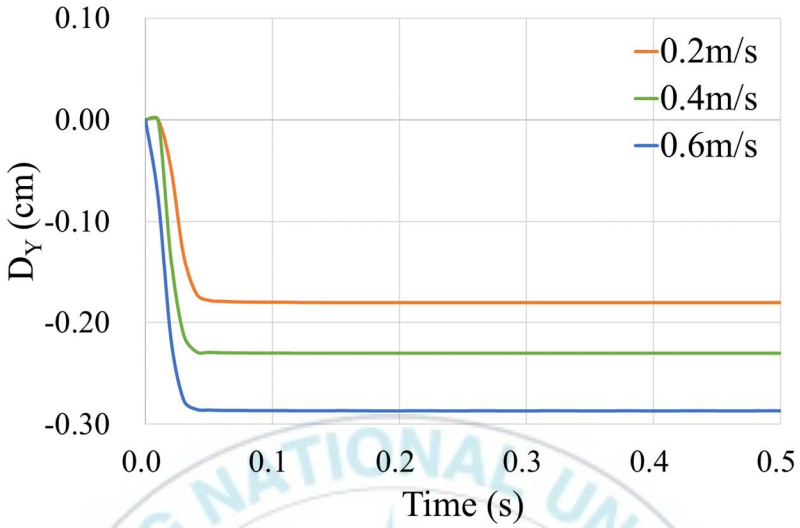

(a) the seabed composed of saturated sand (70%) and gravel (30%)

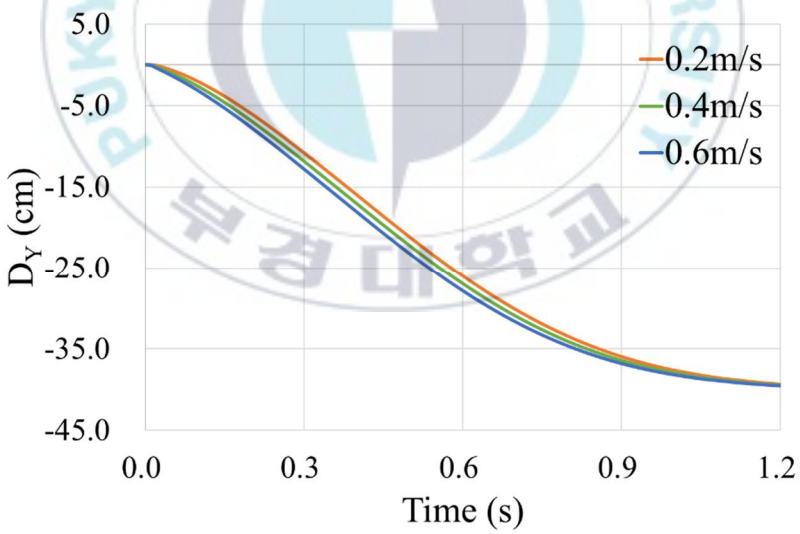

(b) the seabed composed of saturated sand (85%) and clay (15%)

Fig. 4.1. Vertical displacement (D_Y) history of the cube-type reef at gauge 5.

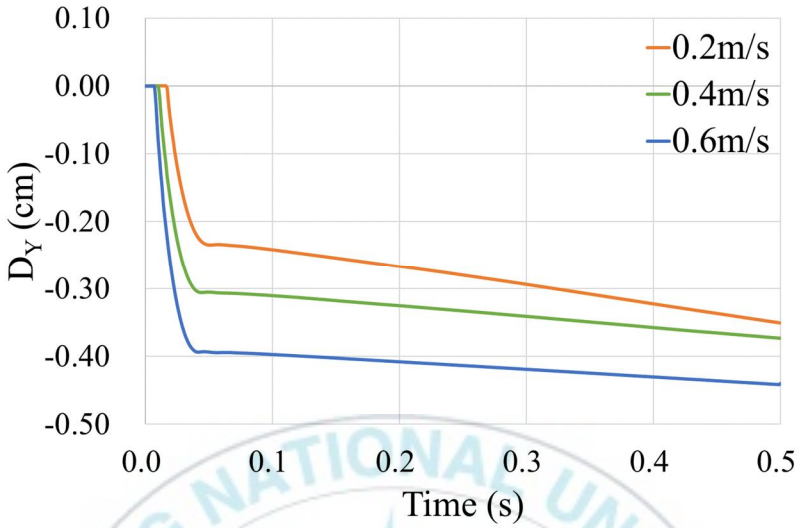

(a) the seabed composed of saturated sand (70%) and gravel (30%)

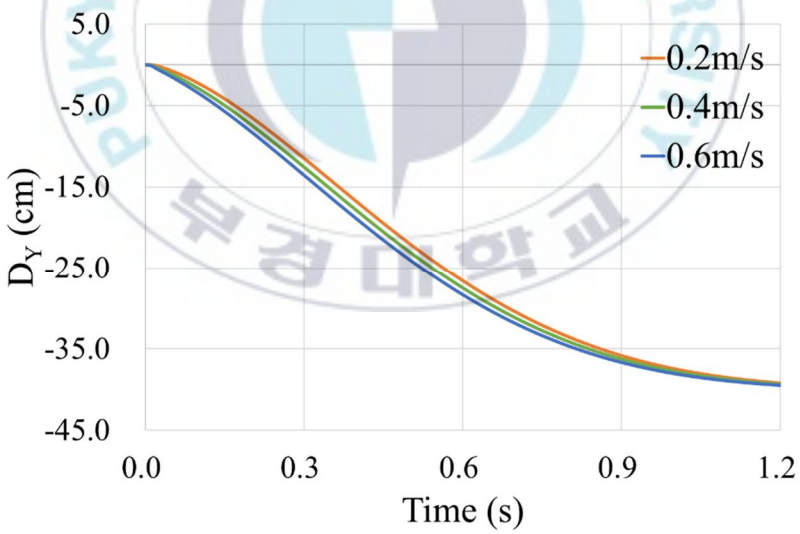

(b) the seabed composed of saturated sand (85%) and clay (15%)

Fig. 4.2. Vertical displacement (D_Y) history of the half-ball type reef at gauge 5.

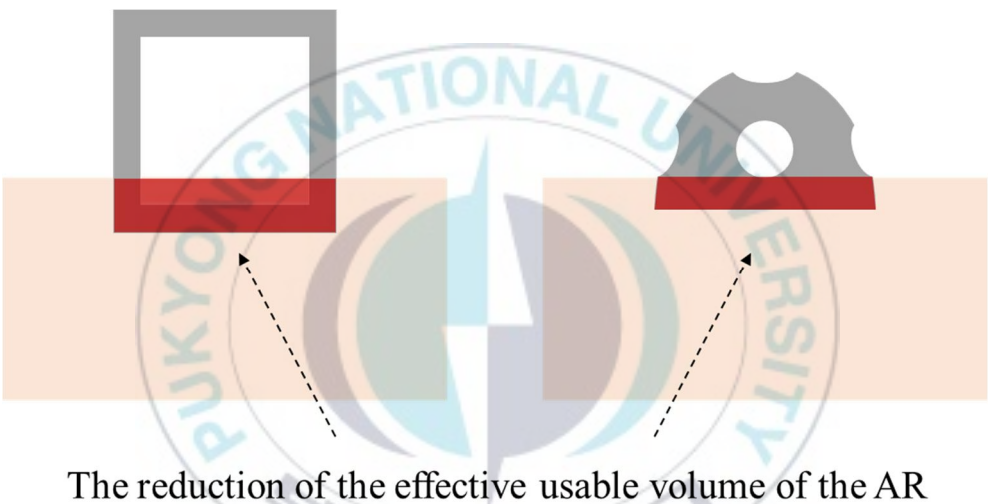

Fig. 4.3. Concept of the reduction of the effective usable volume of the AR.

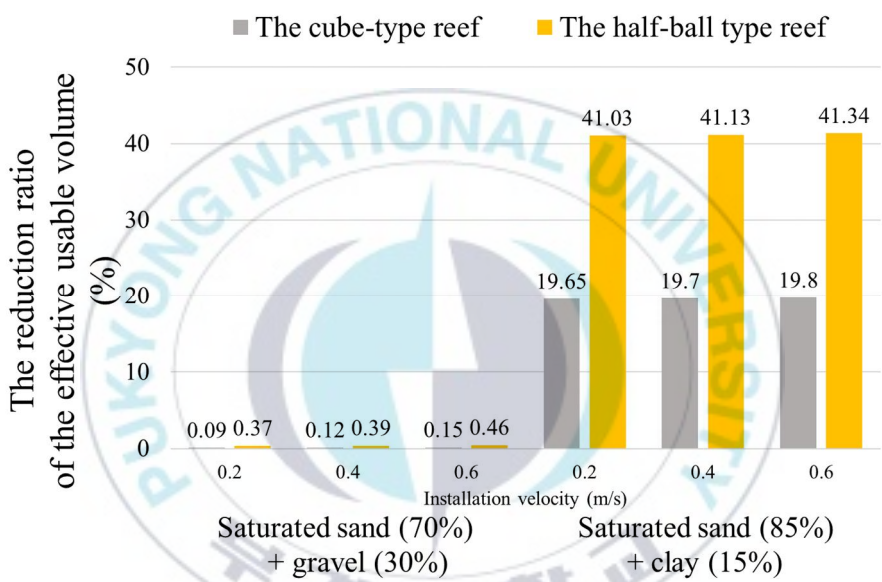

Fig. 4.4. The reduction ratio of the effective usable volume for each case.

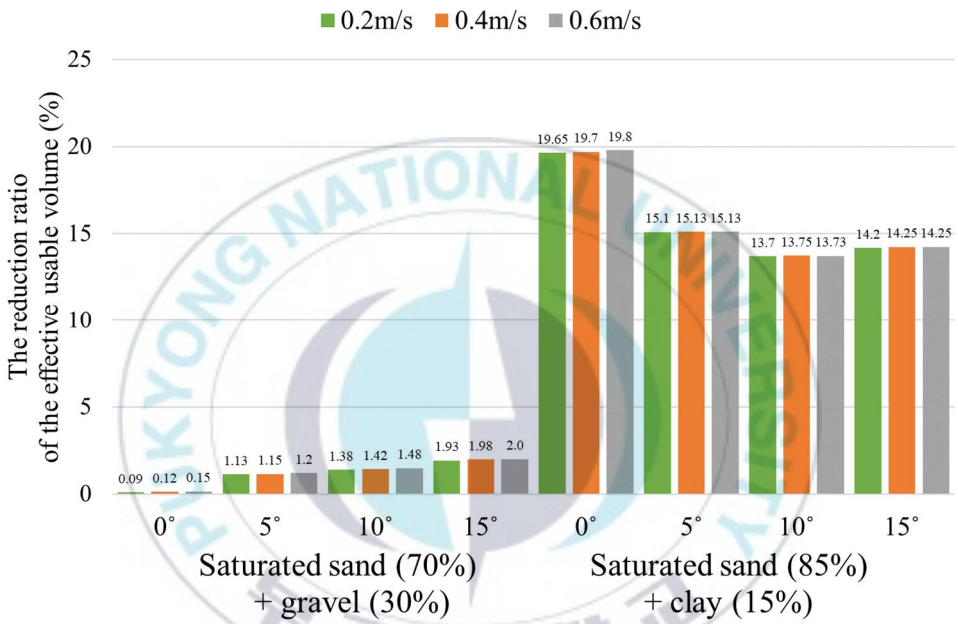

Fig. 4.5. The reduction ratio of the effective usable volume considering the installation angle cases.

CHAPTER 5
CONCLUSIONS

In this study, the settlement of the seabed was estimated to investigate the effect of the collision between the ARs and the seabed conditions during the installation of the ARs. Three installation velocities and two seabed soil conditions were applied to the two ARs. Explicit dynamic collision analyses were carried out by ANSYS AUTODYN. From the collision analysis, the following conclusions were made.

First, if the installation velocity is less than 1m/s during the AR installation with cables, the initial settlements of the seabed conditions are generally similar. Considering those velocities (0.2, 0.4, and 0.6m/s), the settlement quantities of three kind of velocities were not significantly different in four cases: (a) installing the cube-type reef on the seabed composed of saturated sand (70%) and gravel (30%), (b) installing the cube-type reef on the seabed composed of saturated sand (85%) and clay (15%), (c) installing the half-ball type reef on the seabed composed of saturated sand (70%) and gravel (30%), and (d) installing the half-ball type reef on the seabed composed of saturated sand (85%) and clay (15%).

Second, the initial settlement of the seabed increases when the angle of contact with the seabed gradually during installation. Considering those angles (0˚, 5˚, 10˚, 15˚), the initial settlement tended to increase as the angle increases. However, the reduction ratio of effective usable volume for saturate sand (85%) and clay (15%) decreased as the angle increases.

Third, the initial settlement occurs considerably when the ARs are installed on the seabed composed of saturated sand (85%) and clay (15%). Considering the cube-type reef, the settlements of the seabed composed of

saturated sand (85%) and clay (15%) are 39.3cm (installation velocity is 0.2m/s), 39.4cm (installation velocity is 0.4m/s), and 39.6cm (installation velocity is 0.6m/s), respectively. Considering the half-ball type reef, the settlements of the seabed composed of saturated sand (85%) and clay (15%) are 39.2cm (installation velocity is 0.2m/s), 39.3cm (installation velocity is 0.4m/s), and 39.5cm (installation velocity is 0.6m/s), respectively. Both ARs have settlements of about 39cm. Considering the settlement of 39cm, the effective usable volumes of the cube-type and half-ball type reefs decreased about 20% and 41%, respectively. These decreases can be considered a tremendous loss of the usable space of ARs for marine fauna and flora, and it is expected to require reinforcement of the seabed when ARs are installed on the seabed composed of saturated sand (85%) and clay (15%).

ACKNOWLEDGEMENT

First of all, I would like to express my sincere gratitude to my advisors, Prof. Won-Bae Na, who guided me in this research. I am very grateful for his advice and comments to my research during the time I was doing my Master course. Also I would like to thank to Prof. Jeong-Tae Kim and Prof. Han-Sam Yoon for their generous advice and guidance as examiners.

Secondly I would also like to thank my friends who encouraged me every time I was exhausted. This work would not have possible without their support and encouragement. I would like to thank my colleagues at Solid Materials & Structures Design Lab (SMSDL) who shared a lot of time during the research. Thanks to them, I was able to spend a pleasant master course in the lab.

Most importantly, I would like to express my gratitude to my parents who supported and encouraged me with endless love. Finally, I hope that all of my people will always be happy.

REFERENCES

ANSYS-Inc. (2009), AUTODYN USER MANUAL VERSION 12.0

Borrvall, T., and Riedel, W., 2011. The RHT concrete model in LS-DYNA, In Proceedings of the 8th European LS-DYNA Users Conference, Strasbourg.

Bragov, A.M., Lomunov, A.K., Sergeichev, I.V., Tsembelis, K., and Proud, W.G., 2008. Determination of physicomechanical properties of soft soils from medium to high strain rates, International Journal of Impact Engineering, 35(9), 967-976.

Chapman, D.J., Tsembelis, K., and Proud, W.G., 2006. The behavior of water saturated sand under shock-loading, In Proceedings of the 2006 SEM Annual Conference and Exposition on Experimental and applied mechanics (Vol. 2, pp. 834-840).

Düzbastılar, F.O., and Şentürk, U., 2009. Determining the weights of two types of artificial reefs required to resist wave action in different water depths and bottom slopes, Ocean Engineering, 36(12), 900-913.

Grujicic, M., and Bell, W.C., 2011. A computational analysis of survivability of a pick-up truck subjected to mine detonation loads, Multidiscipline Modeling in Materials and Structures, 7(4), 386-423.

Grujicic, M., Pandurangan, B., Summers, J. D., Cheeseman, B.A., Roy, W. N., and Skaggs, R.R., 2008. Application of the modified compaction material

model to the analysis of landmine detonation in soil with various degrees of water saturation, Shock and Vibration, 15(1), 79-99.

Grujicic, M., Pandurangan, B., Huang, Y., Cheeseman, B.A., Roy, W.N., and Skaggs, R.R., 2007. Impulse loading resulting from shallow buried explosives in water-saturated sand, In Proceedings of the Institution of Mechanical Engineers, Part L: Journal of Materials Design and Applications, 221(1), 21-35.

Han, S., 2016. Estimation of seabed settlement and impact force for a box-type artificial reef considering seabed soil conditions in the initial installation procedure. Master's Thesis, Pukyong National University.

Jung, S., Kim, D., Na, W.B., 2016. Wake volume characteristics considering artificial reef canyon intervals constructed by flatly distributed artificial reef set, Journal of Ocean Engineering and Technology, 30(3), 169-176.

Kim, T., Kim, C., Kim, D., 2008. Development of coastal zone by artificial reef, Chonnam National University Press.

Kim, D.K., Suh, S.H., Cho, J.K., Kim, C.G., Choi, I.H., Kim, B.S., 2009. Settlement Characteristics of Square Reefs installed on Soft Seafloor Ground, Journal of the Korean Society of Marine Engineering, 34(1), 163-167.

Korea Fisheries Resources Agency (FIRA), 2017a. The Status of Artificial Reef.

Korea Fisheries Resources Agency (FIRA), 2017b. The Statistics of Artificial Reef Installation.

Laine, L., and Sandvik, A., 2001. Derivation of mechanical properties for sand, In Proceedings of the 4th Asia-Pacific Conference on Shock and impact loads on structures, CI-Premier PTE LTD, Singapore (Vol. 361, p. 368). ANSYS Inc.

Woo, J., Kim, D., Yoon, H.S., and Na, W.B., 2014. Characterizing Korean general artificial reefs by drag coefficients, Ocean Engineering, 82, 105-114.

Woo, J., Na, W.B., Kim, H.T., 2009. Numerical Simulation of Arch-type Submarine Cable Protector under Anchor Collision, Journal of Ocean Engineering and Technology, 23(1), 96-103.

Yoon, H.S., Kim, D., Na, W.B., 2016. Estimation of effective usable and burial volumes of artificial reefs and the prediction of cost-effective management, Ocean & Coastal Management, Vol. 120, pp. 135-147.